RESEARCH ARTICLE

Mutant IDH Inhibits IFNγ–TET2 Signaling to Promote Immunoevasion and Tumor Maintenance in Cholangiocarcinoma

Meng-Ju Wu[1,2], Lei Shi[1,2], Juan Dubrot[2,3], Joshua Merritt[1], Vindhya Vijay[1], Ting-Yu Wei[1], Emily Kessler[2,3], Kira E. Olander[2,3], Ramzi Adil[1], Amaya Pankaj[1,4], Krishna Seshu Tummala[1], Vajira Weeresekara[1], Yuanli Zhen[1], Qibiao Wu[1], Meiqi Luo[5], William Shen[6], María García-Beccaria[7], Mirian Fernández-Vaquero[7], Christine Hudson[8], Sebastien Ronseaux[8], Yi Sun[1], Rodrigo Saad-Berreta[1], Russell W. Jenkins[1], Tong Wang[9], Mathias Heikenwälder[7], Cristina R. Ferrone[10], Lipika Goyal[1], Brandon Nicolay[8], Vikram Deshpande[1,4], Rahul M. Kohli[5,11], Hongwu Zheng[12], Robert T. Manguso[2,3], and Nabeel Bardeesy[1,2]

ABSTRACT Isocitrate dehydrogenase 1 mutations (mIDH1) are common in cholangiocarcinoma. (R)-2-hydroxyglutarate generated by the mIDH1 enzyme inhibits multiple α-ketoglutarate–dependent enzymes, altering epigenetics and metabolism. Here, by developing mIDH1-driven genetically engineered mouse models, we show that mIDH1 supports cholangiocarcinoma tumor maintenance through an immunoevasion program centered on dual (R)-2-hydroxyglutarate–mediated mechanisms: suppression of $CD8^+$ T-cell activity and tumor cell–autonomous inactivation of TET2 DNA demethylase. Pharmacologic mIDH1 inhibition stimulates $CD8^+$ T-cell recruitment and interferon γ (IFNγ) expression and promotes TET2-dependent induction of IFNγ response genes in tumor cells. $CD8^+$ T-cell depletion or tumor cell–specific ablation of TET2 or IFNγ receptor 1 causes treatment resistance. Whereas immune-checkpoint activation limits mIDH1 inhibitor efficacy, CTLA4 blockade overcomes immunosuppression, providing therapeutic synergy. The findings in this mouse model of cholangiocarcinoma demonstrate that immune function and the IFNγ–TET2 axis are essential for response to mIDH1 inhibition and suggest a novel strategy for potentiating efficacy.

SIGNIFICANCE: Mutant IDH1 inhibition stimulates cytotoxic T-cell function and derepression of the DNA demethylating enzyme TET2, which is required for tumor cells to respond to IFNγ. The discovery of mechanisms of treatment efficacy and the identification of synergy by combined CTLA4 blockade provide the foundation for new therapeutic strategies.

See related commentary by Zhu and Kwong, p. 604.

INTRODUCTION

IDH1 is the most commonly mutated metabolic gene across human cancers, with highest mutational frequency observed in acute myeloid leukemia (AML), glioma, chondrosarcoma, and intrahepatic cholangiocarcinoma (ICC; cancer of liver bile ducts; refs. 1–4). Mutations of the hotspot R132 codon alter the activity of the IDH1 enzyme, resulting in the NADPH-dependent conversion of α-ketoglutarate to (R)-2-hydroxyglutarate [(R)-2HG], which accumulates to millimolecular levels within tumors (5, 6). (R)-2HG competitively inhibits a range of enzymes that utilize α-ketoglutarate (7–9). Targets include the JmjC family histone demethylases and TET family DNA demethylases (2, 8, 10) whose inhibition is linked to the altered epigenetic state characteristic of many mIDH tumors. Additional (R)-2HG targets participate in diverse biological processes, including amino acid and RNA metabolism (BCAT transaminases; ref. 11), collagen maturation (12), DNA repair (13, 14), mTOR signaling (15), and hypoxic response (16). (R)-2HG has also been implicated in immunosuppression via both transcriptional control of cytokine production in tumor cells and direct paracrine effects of secreted (R)-2HG on various immune cell types (17–20). Because cancer-associated mutational variants at $IDH1^{R132}$ differ markedly in their (R)-2HG generating activity (5, 21–23) and because the reported inhibitory values for candidate targets span a wide (R)-2HG concentration range (8, 9), there may be significant context specificity to the outputs of mutant IDH. Overall, the pleiotropic effects of (R)-2HG have complicated the elucidation of the molecular targets and resulting biological processes by which mIDH drives tumor initiation and potentially contributes to maintenance of advanced tumors in different tissues.

Pharmacologic inhibition of mIDH in human cancers has shown variable efficacy, the mechanistic basis of which requires further study. In AML, the requirement for mIDH in sustained tumor growth is well established, and selective small-molecule mIDH1 and mIDH2 inhibitors have received regulatory approval in this setting (24). The frequent complete remissions upon mIDH inhibitor treatment and acquisition of secondary IDH mutations as a clinical resistance mechanism highlight the oncogene addiction phenotype driven by mIDH in AML

[1]Cancer Center, Massachusetts General Hospital, Boston, Massachusetts; Department of Medicine, Harvard Medical School, Boston, Massachusetts. [2]Broad Institute of Harvard and Massachusetts Institute of Technology, Cambridge, Massachusetts. [3]Cancer Center, Massachusetts General Hospital, Harvard Medical School, Charlestown, Massachusetts. [4]Department of Pathology, Harvard Medical School, Boston, Massachusetts. [5]Department of Biochemistry and Biophysics, University of Pennsylvania, Philadelphia, Pennsylvania. [6]Cancer Center, Massachusetts General Hospital, Boston, Massachusetts; Harvard University, Boston, Massachusetts. [7]Division of Chronic Inflammation and Cancer, German Cancer Research Center (DKFZ), Heidelberg, Germany. [8]Agios Pharmaceuticals, Cambridge, Massachusetts. [9]Graduate Group in Biochemistry and Molecular Biophysics, University of Pennsylvania, Philadelphia, Pennsylvania. [10]Department of Surgery, Harvard Medical School, Boston, Massachusetts. [11]Department of Medicine, University of Pennsylvania, Philadelphia, Pennsylvania. [12]Pathology and Laboratory Medicine, Weill Cornell Medicine, New York, New York.

Note: Supplementary data for this article are available at Cancer Discovery Online (http://cancerdiscovery.aacrjournals.org/).

M.-J. Wu, L. Shi, and J. Dubrot contributed equally to this article.

Corresponding Authors: Nabeel Bardeesy, Massachusetts General Hospital Cancer Center, Harvard Medical School, 185 Cambridge Street, CPZN 4216, Boston, MA 02114. Phone: 617-643-2579; E-mail: Bardeesy.Nabeel@mgh.harvard.edu; and Robert T. Manguso, Broad Institute of MIT and Harvard, 415 Main Street, Room 4019, Cambridge, MA 02142. Phone: 508-498-0837; E-mail: rmanguso@broadinstitute.org

Cancer Discov 2022;12:812–35

doi: 10.1158/2159-8290.CD-21-1077

(25). Responses are associated with differentiation of the leukemic stem cells to mature myeloid cells, pointing to mIDH inhibition as a form of differentiation-based therapy (26–28). mIDH has also been shown to influence cell-fate decisions in multiple additional tissues, including the liver (23, 29–31). However, the functions of mIDH in the maintenance of ICC and other solid tumors remain unclear. Although mIDH1 inhibition provides clinical benefit for patients with ICC and glioma, this strategy typically delays progression rather than significantly shrinking tumors, and the efficacy is often short-lived (32–34). Moreover, mIDH inhibition has not produced consistent or robust responses in different solid tumor model systems, and several studies report that the mutant *IDH* allele is selectively lost upon malignant progression or limits initial tumor growth (35–38). In this regard, (R)-2HG has been shown to suppress DNA repair and promote genomic instability—effects consistent with greater impact on tumor initiation than maintenance. These observations have motivated the search for alternative therapeutic strategies, which, rather than inhibiting the mutant enzyme, harness the alterations in cellular circuitry resulting from high (R)-2HG levels (11, 14, 39–43).

A potential limitation of prior experimental studies on the roles of mIDH in the sustained growth of advanced solid malignancies relates to the available model systems, including xenografts and cell line or spheroid models as well as engineered cancer models in which ectopic mIDH1 expression does not contribute to tumor initiation, which may not fully recapitulate relevant biological features of native tumors. Here, we report the generation of genetically engineered mouse models (GEMM) to probe the functions of mutant IDH1 in ICC pathogenesis. Using a GEMM where mutant IDH1 strongly promotes the development of ICC and associated allografts models, we establish a central (R)-2HG–controlled pathway coordinating epigenetic reprogramming and immune escape, whose inhibition potentiates responsiveness to immunotherapy.

RESULTS

Selective Induction of Murine ICC by the High (R)-2HG–Producing *Idh1*^{R132C} Allele

The profile of mutational variants at the hotspot IDH1 R132 codon differs across human cancer types, with R132C representing >70% of mIDH1 ICCs compared with R132H, which has <1% incidence in ICC but is prevalent in glioma (Fig. 1A). To assess the capacity of these mIDH1 variants to promote ICC in GEM, we developed latent knock-in alleles of both *Idh1*^{R132H} and *Idh1*^{R132C} in which expression of the mutant alleles from the endogenous locus is controlled by a floxed STOP cassette (Fig. 1B; Supplementary Fig. S1A; Methods). These strains were crossed to *Alb-Cre* transgenic mice to generate animals with liver-specific activation of mutant IDH1, designated the C (*Alb-Cre*), CI^{R132C} (*Alb-Cre*; *Idh1*^{R132C}), and CI^{R132H} (*Alb-Cre*; *Idh1*^{R132H}) cohorts. The compound mutant mice were born at the expected Mendelian frequency and without overt pathology. Examination of livers at 11 weeks confirmed that (R)-2HG concentrations were markedly elevated upon mIDH1 expression, with particularly high levels produced by the *Idh1*^{R132C} allele [median concentration of (R)-2HG: *C*: 0.07 nmol/mg; *CI*^{R132H}: 7.8 nmol/mg; *CI*^{R132C}: 35.3 nmol/mg; Supplementary Fig. S1B].

As *IDH1* mutations coexist with activating genetic alterations in different RTK–RAS–MEK pathway genes in approximately 28% of human ICCs—with *KRAS* mutations most common (Supplementary Fig. S1C; data accessed from www.cbioportal.org/genie/; refs. 44–46)—we intercrossed the above strains with LSL-*Kras*^{G12D} mice (Fig. 1B) to establish the CK (*Alb-Cre*; *Kras*^{G12D}), CKI^{R132H} (*Alb-Cre*; *Kras*^{G12D}; *Idh1*^{R132H}), and CKI^{R132C} (*Alb-Cre*; *Kras*^{G12D}; *Idh1*^{R132C}) cohorts. As seen in the single-mutant strains, *Idh1*^{R132C} produced much greater levels of hepatic (R)-2HG than *Idh1*^{R132H} in the context of *Kras*^{G12D} (Fig. 1C). Longitudinal monitoring of these animals revealed pronounced cooperativity between *Idh1*^{R132C} and *Kras*^{G12D} in promoting aggressive ICC. CKI^{R132C} mice developed poor body condition and palpable liver masses requiring euthanasia between 27 and 54 weeks (median tumor-free survival: 49.3 weeks; Fig. 1D; Supplementary Fig. S1D and S1E). Necropsy demonstrated multifocal liver tumors (Fig. 1E) with pancreatic, lung, kidney, and/or peritoneal metastases observed in 20.4% of mice (Fig. 1F; Supplementary Fig. S1F). Histopathologic analysis and CK19 staining established ICC with similar morphologic features to human mIDH1 ICC as the main tumor phenotype in 68.5% of the animals, with the rest typically showing foci of ICC against the backdrop of hepatocellular carcinoma (HCC) histology (Fig. 1G and H; Supplementary Figs. S1G and S2A–S2D); all metastases had ICC histology (Fig. 1I; Supplementary Fig. S1F). By contrast, most CK, CI^{R132C}, and CI^{R132H} mice remained tumor-free for >90 weeks, and, when tumors were observed, they exhibited HCC features as the predominant malignant phenotype with minor presence of ICC (of tumor-bearing CK, CI^{R132C}, and CI^{R132H} mice, 6.9%, 0%, and 0% showed mainly ICC pathology, respectively; Supplementary Figs. S1D, S1G, and S2D). In addition, hepatomegaly was common and eventually necessitated euthanasia of subsets of these animals without evidence of neoplasia. CKI^{R132H} mice exhibited intermediate features, with a tumor-free survival of 60.2 weeks, and a phenotype dominated by HCC (92.3% of tumor-bearing mice) with very rare presence of frank ICC (7.7% of mice; Fig. 1D; Supplementary Figs. S1G and S2B). Unlike the CKI^{R132C} cohort, metastases were not observed in any of the other genotypes (Supplementary Fig. S1F). Serial analysis of mice at time points prior to clinical evidence of disease reinforced the selective capacity of IDH1^{R132C} to incite ICC development, with CKI^{R132C} livers exhibiting biliary atypia [oval cell proliferation (OCP)] and precursor lesions [biliary adenomatous neoplasia (BAN)], contiguous with incipient ICC (Fig. 1J). Collectively, these results demonstrate a specific and potent role of IDH1^{R132C} in driving invasive and metastatic ICC in a GEMM that effectively recapitulates the histopathogenesis of the human disease. The distinct ability of IDH1^{R132C} to promote ICC compared with IDH1^{R132H} is in accord with the relative frequencies of these alleles in human ICC, indicating cross-species conservation of tumorigenic mechanisms and suggesting a requirement for the very high (R)-2HG levels generated by IDH1^{R132C} to elicit ICC development.

mIDH1 Inhibition Stimulates IFNγ Response and Requires Intact Immune Function for Efficacy

In order to have a tractable system to study the functions of mutant IDH1 in the growth of advanced ICC, we established

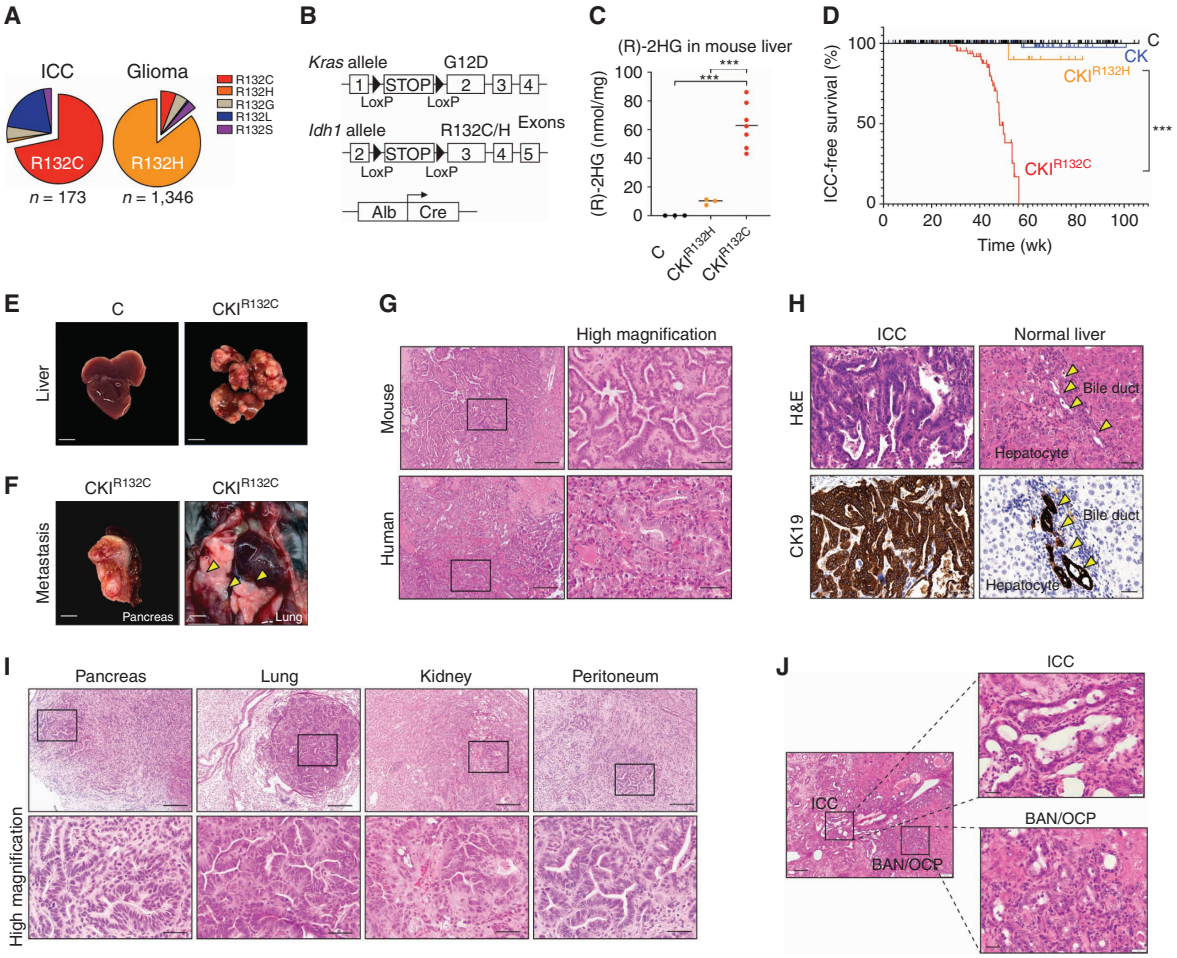

Figure 1. Development of an IDH1^{R132C}-driven GEMM of ICC. **A,** Relative frequency of *IDH1*-mutant variants in human ICC and glioma (data obtained from AACR Project GENIE). **B,** Schematic of mouse strains. **C,** Concentration of (R)-2HG in livers from mice with the indicated genotypes at 11 weeks of age detected by a colorimetric (R)-2HG assay kit. C: $N = 3$; CKI^{R132H}: $N = 3$; CKI^{R132C}: $N = 7$ (N, mouse numbers). **D,** Kaplan–Meier analysis for time until ICC tumor progression necessitated euthanasia. C: $N = 263$; CK: $N = 125$; CKI^{R132H}: $N = 18$; CKI^{R132C}: $N = 108$ (N, mouse numbers). Kaplan–Meier curves were analyzed by the log-rank test. ***, $P < 0.001$ was considered statistically significant. **E,** Representative photographs depicting livers from 43-week-old mice of the indicated genotypes. **F,** Representative gross photographs of metastatic tumors from CKI^{R132C} mice. **G,** Representative hematoxylin and eosin (H&E)–stained section of ICC from a CKI^{R132C} mouse (top) and a human mIDH1 ICC shown for comparison (bottom). **H,** Tissue sections of ICC and adjacent normal liver from a representative CKI^{R132C} mouse subjected to H&E staining (top) and IHC staining against CK19 (bottom). **I,** H&E-stained sections from CKI^{R132C} mice revealing metastatic spread of ICC to the indicated tissues. Bottom, higher magnification. **J,** H&E-stained sections of precursor BAN and OCP from CKI^{R132C} mice at 35 weeks. The boxed regions on the left are shown in higher magnification on the right. Scale bars: 1 cm (**E**), 2 mm (**F**), 200 μm (**G,** top left; **I**, top), 100 μm (**G,** bottom left; **J**, left), 50 μm (**G,** top right; **H**; **I**, bottom), 20 μm (**G,** bottom right; **J**, right).

multiple independent primary ICC cell cultures from the CKI^{R132C} GEMM (Supplementary Fig. S3A). We confirmed that these cell lines produced greatly elevated levels of 2HG as compared with ICC cell lines derived from a separate GEMM that harbors wild-type IDH alleles [*Alb-Cre*; *Kras*^{G12D}; *p53*$^{flox/+}$ (CKP); ref. 47; Supplementary Fig. S3B]. Subcutaneous or orthotopic (intrahepatic) injection of CKI^{R132C} ICC cells into immune-competent syngeneic animals resulted in allograft tumors with close histopathologic similarity to the tumors arising natively in the GEMM (Fig. 2A and B).

We next used the ICC cell cultures and allografts to investigate the response to pharmacologic inhibition of mIDH1 *in vitro* and *in vivo* (Fig. 2C). Under standard *in vitro* culture conditions, CKI^{R132C} ICC cells showed no change in viability upon treatment with the selective mIDH1 inhibitor AG120 (1 μmol/L), despite reducing (R)-2HG levels by 96% (Supplementary Fig. S3C and S3D).

For *in vivo* studies, mice bearing tumors ~100 mm^3 were administered 150 mg/kg AG120 twice/daily, which mimicked the pharmacokinetics and pharmacodynamics observed at the clinical dose in humans (48), including durable reduction in intratumoral (R)-2HG by 95% (Fig. 2D; Supplementary Fig. S3E–S3L). In contrast to the *in vitro* findings, AG120 treatment slowed growth in two independent subcutaneous

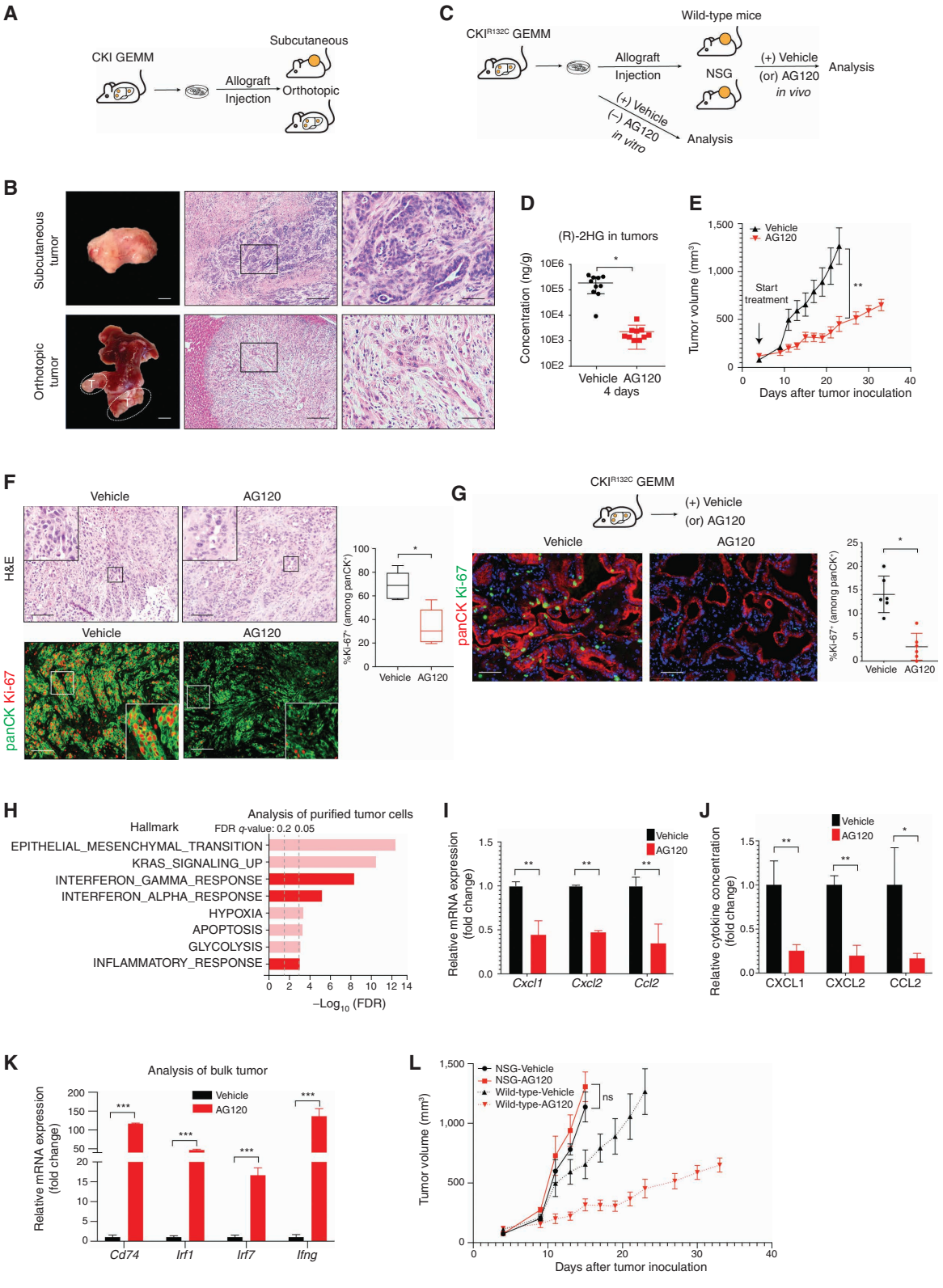

allograft models (2205 and 2275-4; Fig. 2E; Supplementary Fig. S3M). Analysis of tumor specimens after seven days of treatment revealed that AG120 decreased tumor cell proliferation significantly (%Ki-67$^+$/panCK$^+$ cells; Fig. 2F) and induced a degree of cell death (cleaved caspase-3; Supplementary Fig. S3N). The observed disease stabilization, rather than tumor regression, is in line with the human clinical trial data (32, 34). AG120 treatment did not affect tumor growth or proliferation of IDH wild-type ICC allografts (CKP model; Supplementary Fig. S3O), indicating that the responses seen in CKI^{R132C} allografts were due to on-target inhibition of the mutant IDH1 enzyme. Efficacy was also seen in CKI^{R132C} orthotopic allografts, in which AG120 treatment initiated following engraftment resulted in a 3- to 5-fold decrease in tumor volume compared with vehicle after three weeks, accompanied by marked reduction in tumor cell proliferation and increased cell death (Supplementary Fig. S3P–S3R). Importantly, we observed comparable antitumor effects of AG120 against autochthonous ICCs arising in the CKI^{R132C} GEMM. Based on the established kinetics of the model (Fig. 1D–J), mice ages 42 to 45 weeks were examined for palpable abdominal tumors and then randomized to receive AG120 or vehicle (N = 6/group). Analysis after six days revealed significantly lower levels of tumor cell proliferation upon AG120 treatment versus vehicle (3.0% ± 2.8% vs. 14.1% ± 3.9%, respectively; Fig. 2G). Long-term monitoring of the allograft models demonstrated that AG120 extended survival; however, the tumors reached an inflection point after approximately 22 days of treatment and then progressed (Fig. 2E; Supplementary Fig. S3M). Thus, although mIDH1 activity is dispensable for the growth of CKI^{R132C} ICC cells *in vitro*, it is important for tumor maintenance *in vivo*, as AG120 treatment provoked strong suppression of tumor cell proliferation despite the concurrent presence of the potent *Kras*^{G12D} oncogene. Nevertheless, the gradual but consistent development of AG120 insensitivity suggests that adaptive changes eventually lead to mIDH1-independent ICC growth.

To gain insight into the mechanisms underlying the antitumor efficacy of AG120, we conducted RNA-sequencing (RNA-seq) analysis of purified tumor cells. For these studies, the immune-competent 2205 subcutaneous allograft model was treated with AG120 or vehicle for six days, and nontumor cells were removed by magnetic bead sorting (negative selection for CD45$^+$ immune cells, CD31$^+$ endothelial cells, TER119$^+$ erythrocytes, and CD90.2$^+$ fibroblasts). We used gene set enrichment analysis (GSEA) to query the differentially expressed genes against the "Hallmark" database as well as against a curated set of hepatocyte lineage genes, based on prior studies linking mIDH to liver fate decisions (23). Consistent with the paradigm that mIDH enforces a differentiation block in cancer cells and, correspondingly, that mIDH inhibition acts as a differentiation therapy, we observed increased expression of hepatocyte marker genes, including targets of the master transcriptional regulator of hepatocyte identity HNF4α [liver-specific genes: normalized enrichment score (NES) = 2.09, FDR q < 0.001; targets of HNF4α: NES = 1.97, FDR q < 0.001; Supplementary Fig. S3S and S3T]. mIDH1 inhibition also led to a comparable or even more pronounced induction of the IFNγ transcriptional response signature (NES = 2.43, FDR q < 10^{-4}) and other inflammatory signatures, which were among the most highly enriched pathways (Fig. 2H). Concomitant with upregulation of IFN signatures upon mIDH1 inhibition, we also observed decreased mRNA and protein levels of tumor-intrinsic chemokines, such as CXCL1, CXCL2, and CCL2 (Fig. 2I and J), which are implicated in restricting lymphocyte infiltration and promoting immune evasion (49–51). IFNγ is mainly produced by tumor-infiltrating T and natural killer (NK) cells (52), and, accordingly, qRT-PCR analysis of RNA from bulk (unsorted) tumor tissue revealed dramatic increases in *Ifng* gene expression upon AG120 treatment and corroborated the increased expression of multiple IFNγ response genes (Fig. 2K). Collectively, these gene-expression data indicate that mIDH1 inhibition promotes features of hepatocyte differentiation in tumor cells while provoking rapid changes in tumor–immune interplay and IFN pathway activation.

We next tested whether such interplay contributes to the efficacy of mIDH1 inhibition by implanting CKI^{R132C} ICC

Figure 2. mIDH1 inhibition in ICC activates IFNγ signaling and requires intact immune function for therapeutic efficacy. **A,** Schematic of development of the CKI^{R132C} allograft tumor model. **B,** Representative images of subcutaneous (top) and orthotopic ICC allografts (bottom). Left, gross photographs; middle, hematoxylin and eosin (H&E) staining. The boxed area is shown at higher magnification at the right. **C,** Approach to studying the response to mIDH1 inhibition *in vitro* and *in vivo*. **D,** LC-MS/MS measurement of relative level of (R)-2HG in ICCs collected 12 hours after the last dose of the four-day treatment. Data, mean±SD. *, P < 0.05; unpaired t test. **E,** Immunocompetent wild-type mice were injected subcutaneously with a CKI^{R132C} primary cell line (2205). When tumors reached ~100 mm^3 in volume, animals were randomized to receive AG120 or vehicle and then analyzed for serial changes in tumor volume. N = 10 mice per group. Data, means ± SEM. **, P < 0.01; unpaired t test. **F,** Representative sections of tumors from mice treated with vehicle or AG120 for seven days. Top, H&E staining. Bottom, immunofluorescence for panCK (green) and Ki-67 (red). Immunofluorescence data are quantified in graph at the right and represent mean±SD. *, P < 0.05. **G,** Top, Schematic of treatment study against autochthonous ICCs arising in the CKI^{R132C} GEMM. Bottom, immunofluorescence staining for Ki-67 (green), panCK (red), and DAPI (blue) in ICCs from CKI^{R132C} mice after six days of treatment with vehicle or AG120. Data are quantified at the right and represent mean±SD. *, P < 0.05; unpaired t test. **H,** GSEA comparing RNA-seq profiles of malignant cells (isolated by magnetic bead–mediated depletion of stromal populations) from subcutaneous allograft tumors from immunocompetent mice treated with AG120 and vehicle for six days. The vertical axis represents eight top ranked pathways in the Hallmark database based on FDR q-values. IFN and inflammatory pathways are highlighted in dark red. The horizontal axis represents $-\log_{10}$FDR of differentially expressed genes in each Hallmark term. **I,** *Cxcl1*, *Cxcl2*, and *Ccl2* mRNA levels in purified malignant cells from AG120-treated and vehicle-treated tumors. Transcript levels were measured as Fragments Per Kilobase of transcript per Million mapped reads (FPKM) values by RNA-seq analysis. Data, mean±SD. **, P < 0.01; unpaired t test. **J,** Bar graphs showing CXCL1, CXCL2, and CCL2 cytokine levels in the medium from tumor spheroids freshly prepared from CKI^{R132C} allografts and cultured for three days in the presence of 1 μmol/L AG120 or vehicle. The cytokine concentrations were measured by Luminex-based multiplex assays. Data, mean ± SD; **, P < 0.01; *, P < 0.05; unpaired t test. **K,** Relative mRNA expression of the indicated genes in vehicle- and AG120-treated bulk (unsorted) tumors. mRNA expression was analyzed by two-step real-time RT-PCR. All data were normalized to *Actb* and then to the geometric mean of vehicle-treated tumors. Data, mean ± SD; ***, P < 0.001; unpaired t test. **L,** Immunodeficient mice (NSG mice) were injected subcutaneously with the CKI^{R132C} primary cell line. When tumors reached ~100 mm^3 in volume, animals were randomized into AG120 (solid red line) and vehicle (solid black line) conditions and analyzed for serial changes in tumor volume. N = 10 mice per group. Data, mean ± SEM; ns, not significant. Dashed lines are data from **E** depicting comparable studies using wild-type mice and shown for comparison. Scale bars, 1 cm (**B**, bottom left), 2 mm (**B**, top left), 200 μm (**B**, middle), 100 μm (**F**), 50 μm (**B**, right; **G**).

cells in immunodeficient NOD-*scid Il2rg*$^{-/-}$ (NSG) mice and assessing AG120 responsiveness. Remarkably, the benefit of AG120 was completely lost in this setting, with tumors growing at identical rates in the AG120- and vehicle-treated groups (Fig. 2L). Thus, the therapeutic effect of mIDH inhibition in ICC requires intact immune function.

Antitumor Efficacy of mIDH1 Inhibition in ICC Is Mediated by CD8$^+$ T-cell Effector Functions

The above findings contrast with observations in AML where clinical response to mIDH inhibition likewise involves induction of tumor cell differentiation, but where the therapeutic efficacy is recapitulated in immunodeficient models (26–28, 53). Although there is limited insight into the mechanisms underlying the therapeutic impact of mIDH inhibition in solid tumors, mIDH and (R)-2HG have emerging roles in immunomodulation. Distinct processes and cell types have been implicated in suppressing antitumor immunity downstream of mIDH, including impaired recruitment of tumor-infiltrating lymphocytes (TIL) due to reduced expression of chemokines by tumor cells and defects in T-cell survival, migration, and effector function due to direct paracrine effects of (R)-2HG (17–20, 54, 55). To determine the effects of mIDH1 inhibition on the immune microenvironment of ICC, we performed single-cell RNA-seq (scRNA-seq) after enrichment of CD45$^+$ cells from orthotopic ICC tumors treated for six days (Supplementary Fig. S4A). We identified 19 cell clusters of the expected lymphoid and myeloid immune subsets in addition to populations of fibroblasts, endothelial cells, adipocytes, and other stromal cells (Supplementary Fig. S4A and S4B). Analysis of cluster dynamics across conditions revealed remarkable changes in the immune composition in AG120-treated tumors. In particular, we observed pronounced alterations in the phenotype and proportions of myeloid cells, including higher frequencies of proinflammatory M1 macrophages and decreased presence of neutrophils and monocytes after mIDH1 inhibition (Supplementary Fig. S4C and S4D), suggesting a shift toward a less immune-suppressive myeloid infiltrate.

Our gene-expression profiling of purified ICC cells from AG120-treated tumors revealed strong enrichment of the IFNγ response gene signature (Fig. 2H). Because IFNγ is produced primarily by tumor-infiltrating T cells and NK cells (Supplementary Fig. S4E), we reclustered the scRNA-seq data to more carefully interrogate these lineages (Fig. 3A). This analysis revealed 10 populations of T or NK cells, including five distinct subsets of CD8$^+$ T cells representing a range of phenotypes from naïve to terminal effector (Fig. 3A; Supplementary Fig. S4F). A comparison of the AG120- to the vehicle-treated condition revealed higher proportions of terminal effector and proliferating CD8$^+$ T cells (*Gzmb*^{high} and *Prf1*^{high}), fewer naïve and Tcf7$^+$ progenitor CD8$^+$ T cells (56–58), and an increased number of NK cells in the AG120-treated condition (Fig. 3A–C; Supplementary Fig. S4F). Moreover, GSEA on CD8$^+$ T cells showed increased effector T-cell gene signatures, cytolytic activity, and IFN response scores after mIDH1 inhibition (Fig. 3D; Supplementary Table S1). To better understand the molecular mechanisms that enhance acquisition of T- and NK-cell effector phenotypes, we also performed GSEA to query the Hallmark database. mIDH1 inhibition markedly enhanced expression of crucial metabolic pathways that support T cell–fate decisions and effector functions, such as oxidative phosphorylation, fatty acid metabolism, and glycolysis in CD8$^+$ T cells (Fig. 3E; Supplementary Fig. S4G and S4H; ref. 55). These differences were more pronounced in effector CD8$^+$ T-cell subsets compared with naïve or TCF7$^+$ progenitor CD8$^+$ T cells (Fig. 3F; Supplementary Fig. S4G). NK cells also exhibited enrichments of signatures of oxidative phosphorylation and fatty acid metabolism, but not glycolysis, and did not show changes in cytolytic activity (Supplementary Fig. S4H).

Based on these observations, we focused on CD8$^+$ T cells for further analysis. The very high levels of (R)-2HG produced by CKI^{R132C} ICCs, as well as the cytokines and other potential metabolic shifts regulated by mIDH1, could mediate cross-talk with immune cells in the tumor microenvironment. In this regard, although (R)-2HG is not cell-permeable, T-cell populations take up this metabolite through their expression of the SLC13A3 transporter (18). Moreover, we found that CD8$^+$ T cells in our mIDH1 ICC allografts accumulate significant amounts of 2HG (Supplementary Fig. S5A). As engagement of glycolysis and mitochondrial fitness is required for T-cell effector function and our GSEA studies revealed evidence of upregulation of these pathways upon mIDH1 inhibition *in vivo*, we examined the impact of mIDH1-controlled secreted factors on the physiology of activated CD8$^+$ T cells *in vitro*. To this end, murine CD8$^+$ T cells were activated by anti-CD3/CD28 antibody beads and subsequently cultured in the presence of either exogenous (R)-2HG or conditioned media from mIDH1 ICC cells grown with or without AG120 treatment. Conditioned media from an IDH1 wild-type (IDH1wt) ICC cell line (CKP) were used as a control. IFNγ, TNFα, and granzyme B production upon restimulation was strongly reduced by exogenous (R)-2HG (Supplementary Fig. S5B–S5D) or by conditioned media from vehicle-treated mIDH1 ICC cells as compared with that from either AG120-treated mIDH1 ICC cells or CKP ICC cells (Supplementary Fig. S5E–S5G). These (R)-2HG–induced impairments in cytokine production were associated with reduced extracellular acidification rate (ECAR; glycolysis) and, to a lesser extent, maximal oxygen consumption rate (mitochondrial fitness) in resting and stimulated CD8$^+$ T cells (Supplementary Fig. S5H and S5I). Therefore, (R)-2HG released from mIDH1 ICC is sufficient to restrict cytokine production and metabolic fitness in activated CD8$^+$ T cells *in vitro*, suggesting a paracrine role for this metabolite in the alterations in CD8$^+$ T-cell effector function observed upon AG120 treatment *in vivo*.

We performed immunostaining for CD8$^+$ cells to complement the scRNA-seq data with spatial information. We first compared tumors from the CKI^{R132C} GEMM with those from the IDH wild-type (IDHwt) CKP GEMM by IHC. Whereas CD8$^+$ cells were readily detected in CKP tumors, CKI^{R132C} tumors showed only sparse staining [78 cells/high-power field (HPF) vs. 20 cells/HPF; Fig. 4A]. Importantly, staining of a collection of 43 primary human tumor samples also demonstrated very low CD8$^+$ T-cell infiltration in mIDH1 ICCs compared with IDHwt ICCs (Fig. 4B). To extend these observations to an independent cohort of human ICCs, we applied the CIBERSORTX tool to predict immune cell abundance from the publicly available International Cancer Genome

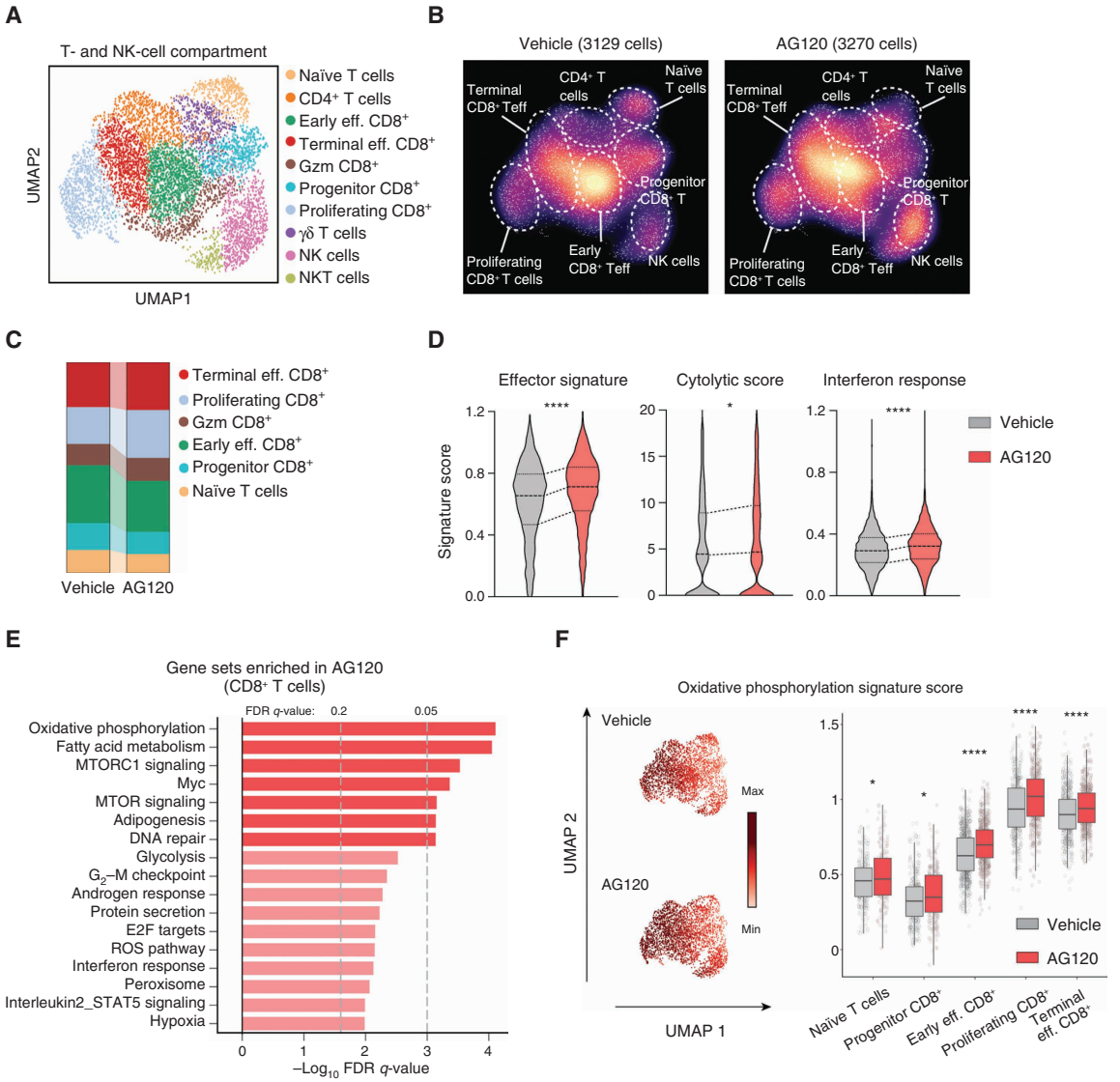

Figure 3. mIDH1 inhibition in ICC promotes CD8+ T-cell effector (eff.) function. **A** and **B,** Identification of tumor-infiltrating T/NK-cell populations. Uniform manifold approximation and projection (UMAP) embeddings of scRNA-seq profiles of CD45+ leukocyte cells from ICC allografts. Representative of one experiment; $N = 4$ pooled vehicle-treated mice and $N = 4$ pooled AG120-treated mice. Teff, effector T cell. **C,** Proportion of different clusters of CD8+ T cells. Gzm, granzyme. **D,** Violin plot indicating effector signatures, cytolytic score, and IFN response signatures. ****, $P < 0.0001$; *, $P < 0.05$. **E,** GSEA of differentially expressed genes (DEG) in CD8+ T cells within tumors from mice treated with AG120 and vehicle for 6 days. The vertical axis represents the 17 top ranked pathways in the Hallmark database with the smallest FDR q-values, and the horizontal axis represents $-\log_{10}$FDR q-values of significantly DEGs in each Hallmark term. **F,** Oxidative phosphorylation signature score in different CD8+ T-cell populations. ****, $P < 0.0001$; *, $P < 0.05$.

Consortium (ICGC) RNA-seq data set (110 total ICC patient samples; ref. 59), which again highlighted the reduced CD8+ T-cell infiltration associated with *IDH* mutations (Fig. 4C). Conversely, AG120 treatment of CKI^{R132C} allograft models for six days resulted in increased total intratumoral CD8+ cells and CD8+ granzyme B+ cytotoxic T cells relative to vehicle control (Fig. 4D; Supplementary Fig. S5J–S5L). Importantly, AG120 stimulated similar T-cell recruitment in autochthonous ICCs arising in the CKI^{R132C} GEMM (Fig. 4E). Thus, mIDH1 ICCs have low numbers of CD8+ T cells with reduced effector function at baseline, whereas AG120 treatment stimulates rapid CD8+ cell infiltration and effector function.

To formally test the requirement for cytotoxic T cells for response to mIDH1 inhibition, we treated mice with anti-CD8 antibody or isotype control prior to generation of subcutaneous allografts and then assessed AG120 efficacy. The results showed that the antitumor activity of AG120 against CKI^{R132C} allografts was completely lost upon CD8+ T-cell depletion, as reflected by tumor volume and cell proliferation measurements (Fig. 4F and G). Collectively, these data reveal

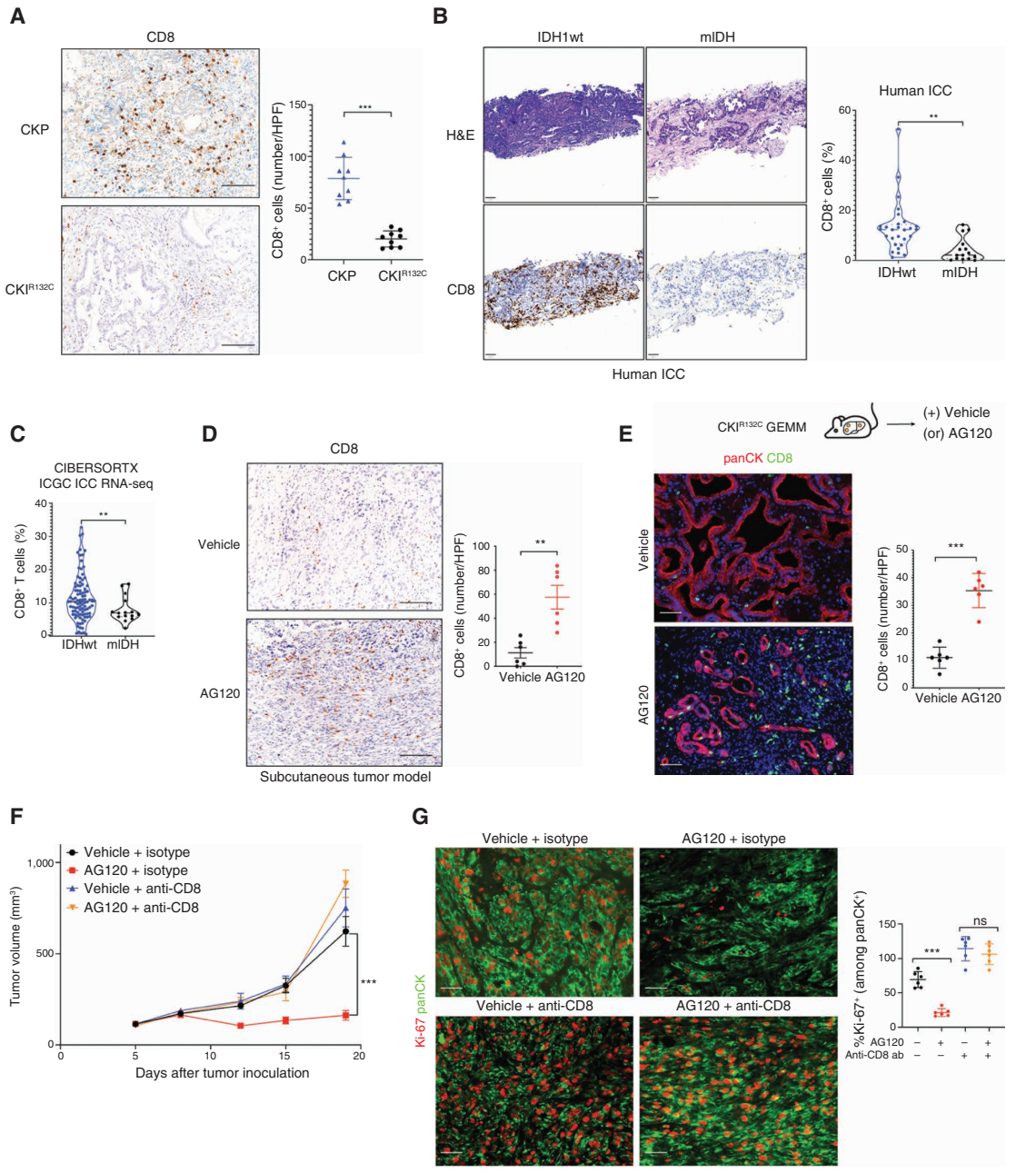

Figure 4. Therapeutic efficacy of mIDH1 inhibition in ICC requires recruitment of tumor-infiltrating CD8+ T cells. **A,** IHC staining for CD8 in ICC from the CKP and CKI^{R132C} GEMMs; right, quantification. $N = 9$ mice/group. Data, mean ± SD; ***, $P < 0.001$; unpaired t test. **B,** Hematoxylin and eosin (H&E) staining (top) and IHC staining for CD8 (bottom) of primary human ICCs with either IDHwt or IDH-mutant genotypes; right, quantification. Data, mean ± SD; **, $P < 0.01$; unpaired t test). **C,** CIBERSORTX analysis of CD8+ T cells in IDHwt ($N = 95$) and mIDH ($N = 15$) ICC in the ICGC expression data set. Total $N = 110$ biologically independent samples. **, $P < 0.01$; unpaired t test. **D,** IHC staining for CD8 in CKI^{R132C} subcutaneous allograft ICCs after six days of treatment with vehicle or AG120; right, quantification. Data, mean ± SD; **, $P < 0.01$; unpaired t test. **E,** Study of CD8+ T-cell infiltrate in ICCs arising autochthonously in the CKI^{R132C} GEMM after 6 days of treatment with vehicle or AG120. Bottom, fluorescence-stained sections; green: CD8, red: panCK, blue: DAPI; right: quantification. Data, mean ± SD; ***, $P < 0.001$; unpaired t test. **F** and **G,** Immunocompetent wild-type mice were injected subcutaneously with a CKI^{R132C} primary ICC cell line. Mice were randomized into two groups and injected with anti-CD8 antibody or isotype control three days before tumor cell inoculation. When tumors reached ~100 mm^3 in volume, animals in each group were randomized into AG120 and vehicle conditions. **F,** Analysis of serial changes in tumor volume. $N = 6$ mice per group. Data, means ± SEM; ***, $P < 0.001$; unpaired t test. **G,** Representative fluorescence-stained sections of tumors following 14 days of treatment with vehicle or AG120; green: panCK, red: Ki-67; right, quantification. Data, mean±SD. ***, $P < 0.001$; ns, not significant; unpaired t test. Scale bars, 100 μm (**A** and **D**) and 50 μm (**B**, **E**, and **G**).

that mIDH1 drives an immunosuppressive phenotype in ICC, and that stimulation of a cytotoxic T cell–mediated immune response is essential for the therapeutic efficacy of AG120.

TET2 Reactivation Is Required for the Antitumor Immunity Induced by mIDH1 Inhibition

The above findings demonstrate a critical role for T-cell immunity in AG120 response of mIDH1 ICCs and point to paracrine immunomodulatory effects of (R)-2HG in this context. However, they leave open the question of whether mIDH1-regulated tumor cell–intrinsic factors are also central to coordinating tumor–immune interplay and growth control. Among candidate (R)-2HG targets, we focused on TET2, which is an established tumor suppressor in AML. The relatively high reported IC_{50} value for inhibition of TET2 by (R)-2HG (7, 8) suggests that TET2 would be strongly compromised in IDH1^{R132C}-expressing livers but only weakly so in the less tumor-prone IDH1^{R132H}-expressing livers based on the observed (R)-2HG levels (Fig. 1C). Although less studied in solid tumors, TET2 has recently been found to hydroxymethylate chemokine gene promoters in complex with STAT1 upon IFNγ stimulation of colon cancer and melanoma cell lines, leading to increased chemokine gene expression and lymphocyte infiltration (Fig. 5A; ref. 60). First, we measured global levels of 5-hydroxymethylcytosine (5hmC) to gauge TET2 activity in tumors from CKP and CKI^{R132C} mice and in the single ICC observed in the CKI^{R132H} model. CKI^{R132C} tumors showed the lowest level of global 5hmC by a wide margin, followed by the CKI^{R132H} model, and then CKP tumors, correlating inversely with relative 2HG concentrations (Fig. 5B; Supplementary Fig. S6A). Importantly, AG120 treatment resulted in a marked (~2-fold) increase in global 5hmC compared with vehicle in CKI^{R132C} tumors (Fig. 5C), directly linking mIDH1 and suppression of TET demethylase activity *in vivo*. In addition, AG120 treatment restored 5hmC levels in both CKI^{R132H} and CKI^{R132C} ICC cells in a dose-dependent manner *in vitro*. Notably, greater AG120 levels were required to restore TET activity in CKI^{R132C} cells, consistent with their 2HG concentrations surpassing the IC_{50} value for TET2 inhibition considerably (0.5 μmol/L AG120 was required to effectively restore 5hmC levels in CKI^{R132C} cells, whereas only 0.1 μmol/L AG120 was required in CKI^{R132H} cells; Supplementary Fig. S6B and S6C).

To examine the specific contribution of TET2 to AG120 response, we deleted *Tet2* (*Tet2* knockout: *Tet2*-KO) in CKI^{R132C} ICC cells using CRISPR–Cas9 genome editing with the selective CRISPR antigen removal (SCAR) vector system (61). This system is optimized for nonimmunogenic lentiviral engineering of target cells. Two *Tet2*-KO lines were generated using distinct single-guide RNAs (sgRNA; sg*Tet2*-1, sg*Tet2*-2; Supplementary Fig. S6D and S6E). sg*Tet2* and sgControl cells were treated *in vitro* with IFNγ and AG120, alone or in combination, to test whether mIDH1 causes cell-autonomous defects in IFNγ response and, correspondingly, whether TET2 reactivation is required for stimulation of IFNγ target genes in the setting of mIDH1 inhibition.

Hydroxymethylated DNA immunoprecipitation qPCR showed that 5hmC levels at the *Irf1* and *Cd274* promoters were increased in sgControl ICC cells upon treatment with AG120, but not with IFNγ, whereas the combination led to a further boost in 5hmC (Fig. 5D). By contrast, in *Tet2*-KO CKI^{R132C} ICC cells, baseline levels of these modifications were barely detectable, and no significant effects of AG120 and IFNγ were seen (Fig. 5D). Accordingly, CKI^{R132C} ICC cells showed an attenuated induction of *Irf1* and *Cd274* mRNA expression in response to IFNγ treatment as compared with CKP ICC cells (Fig. 5E). AG120 potentiated IFNγ-mediated stimulation of these genes in CKI^{R132C} ICC cells, an effect abolished (*Irf1*) or partially overcome (*Cd274*) by *Tet2* deletion (Fig. 5E). *Tet2* deletion did not reduce phosphorylation of STAT1 (Supplementary Fig. S6F). Thus, mIDH1 blocks induction of IFNγ target genes in ICC cells due to 2HG-dependent inhibition of TET2, whereas upstream IFNγ receptor–JAK–STAT1 signaling remains intact.

We next corroborated these findings in a set of human cholangiocarcinoma cell lines, including two with wild-type IDH1/IDH2 (ICC15 and ICC18) and two with mutant IDH1 (RBE and SNU1079). mIDH1 cholangiocarcinoma cell lines had low 5hmC levels relative to the wild-type cholangiocarcinoma cell lines, whereas AG120 treatment strongly boosted 5hmC levels in the mIDH1 cells (Supplementary Fig. S6G). Moreover, whereas the IDH1wt cell lines were highly responsive to IFNγ treatment, showing pronounced upregulation of established target genes (15–30-fold induction of *IRF1*, *CD274*, and *IFIT3*), the mIDH1 lines showed muted response (most with less than twofold induction; Supplementary Fig. S6H). Importantly, AG120 treatment significantly enhanced the response of mIDH1 cells to IFNγ. Thus, mIDH1 leads to defects in TET activity and IFNγ response in human ICC cells—effects that are reversed by mIDH1 inhibition.

Next, we tested the impact of TET2 status on AG120 response *in vivo* by generating syngeneic immunocompetent mouse models using mIDH1 ICC sgControl cells and mIDH1 ICC *Tet2*-KO (sg*Tet2*-1 and sg*Tet2*–2) cells. Consistent with our prior studies, AG120 treatment slowed progression and induced cell death (cleaved caspase-3) of mIDH1 ICC-control tumors, whereas the mIDH1 ICC-*Tet2*-KO tumors were completely unaffected (Fig. 5F and G). However, both the recruitment of CD8$^+$ T cells and induction of IFNγ expression in the bulk tumor were increased by AG120 regardless of TET2 status in the malignant cells (Supplementary Fig. S7A and S7B). Moreover, IHC staining revealed that total nuclear STAT1 and phosphorylated STAT1 were increased upon mIDH1 inhibition in the tumors in both the control and *Tet2*-KO groups (Supplementary Fig. S7C). Thus, TET2 reactivation is essential for the therapeutic efficacy of AG120 but is dispensable for stimulation of the upstream induction of IFNγ signaling.

We used the NanoString Immune Profiling gene-expression platform to investigate the contributions of TET2 to the tumor-intrinsic immune response resulting from mIDH1 inhibition *in vivo*. This analysis surveyed 770 immune-related genes in magnetic bead–purified tumor cells from the mIDH1 ICC control and mIDH1 ICC *Tet2*-KO models after five days of treatment with AG120 or vehicle. Among the annotated set of 93 IFNγ-stimulated genes, 37 were induced >2-fold (and 54 were >1.5-fold) after AG120 treatment in mIDH1 ICC sgControl tumor cells, whereas none were induced by AG120 in the mIDH1 ICC-*Tet2*-KO model (Fig. 5H shows a heat map of IFNγ-stimulated genes; Supplementary Fig. S7D shows

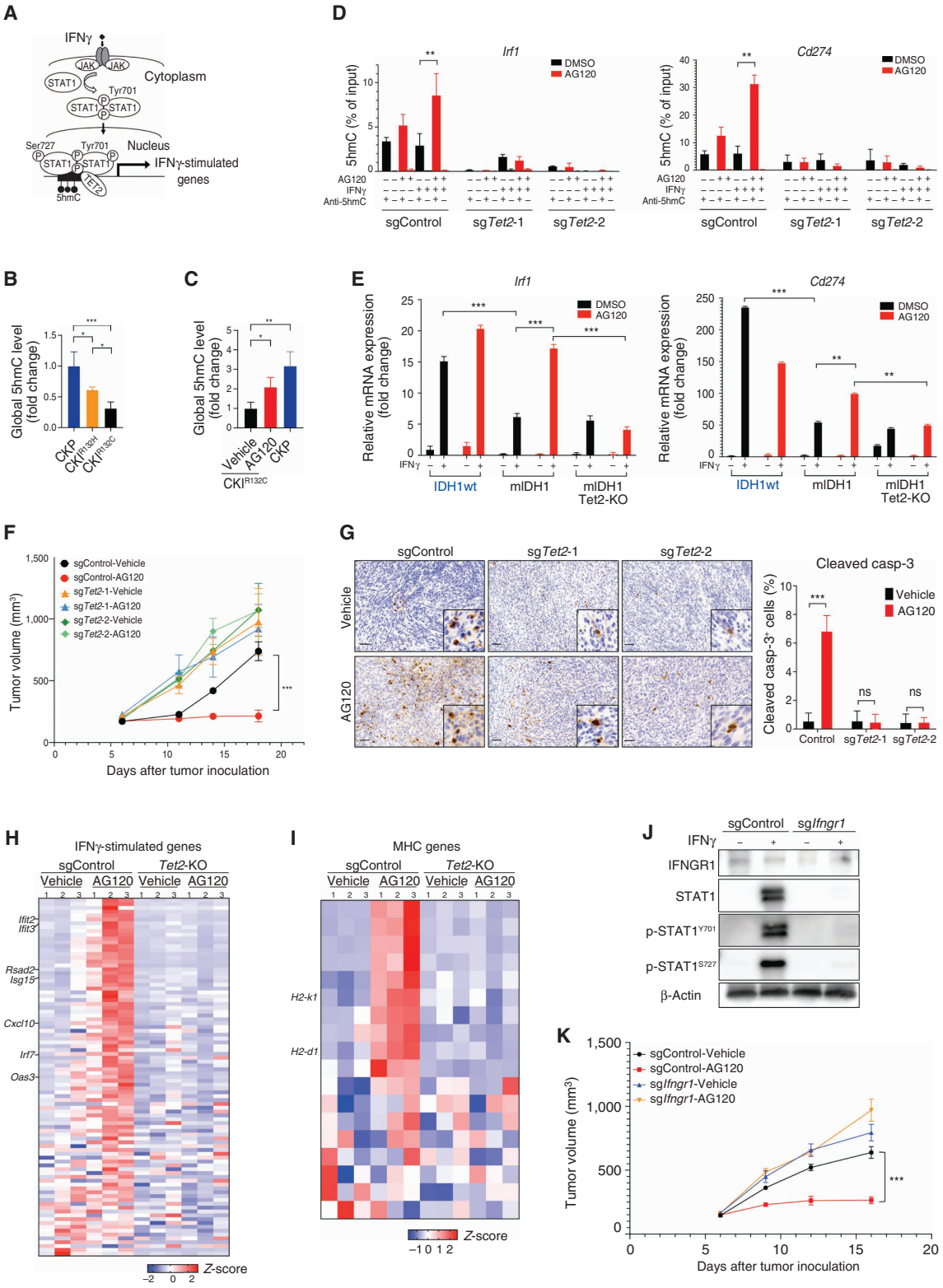

representative genes). The IFNγ response pathway remained upregulated in ICC cells in a TET2-dependent manner after 15 days of treatment, as demonstrated by targeted RT-qPCR analysis (Supplementary Fig. S7E). These observations support a key role of TET2 in mediating tumor cell response to mIDH1 inhibition by epigenetically activating IFNγ target genes *in vivo*.

IFNγ signaling can stimulate specific antitumor immune responses by upregulating expression of MHC class I or II molecules on tumor cells. We found that mIDH1 inhibition in ICC allografts led to the prominent TET2-dependent upregulation of a broad set of MHC genes (e.g., *H2-k1* and *H2-d1*; Fig. 5I). Moreover, in the context of IFNγ treatment, mIDH1 inhibition increased MHCI ($H2^{Kb}/H2^{Db}$) at the cell surface in sgControl cells, but not in sg*Tet2* cells (Supplementary Fig. S7F). These data implicate IFNγ–TET2-mediated induction of MHCI in the AG120 response. We engineered CKI^{R132C} ICC cells with SCAR-mediated deletion of IFNγ receptor 1 (*Ifngr1*-KO) to formally test the requirement for IFNγ signaling in AG120 efficacy. Importantly, as observed for Tet2 deletion, allografts established from *Ifngr1*-KO ICC cells were resistant to AG120 (Fig. 5J and K). Collectively, these data point to dual mechanisms by which mIDH1 inhibition restores antitumor immunity in ICC, involving increased $CD8^+$ T-cell infiltration and effector function as well as reactivation of TET2 to enable the IFNγ-induced epigenetic response program in the malignant cells. Notably, NanoString profiling of a custom panel of hepatocyte lineage genes showed that TET2 inactivation did not compromise the hepatocyte marker induction caused by AG120 treatment (Supplementary Fig. S7G), consistent with the primacy of immune cross-talk rather than cellular differentiation in therapeutic efficacy.

Anti-CTLA4 Synergizes with mIDH1 Inhibition by Overcoming IFNγ-Induced Checkpoints

The antitumor effects of the IFNγ signaling can be limited by feedback activation of checkpoints, which ultimately compromise immune responses, suggesting a possible explanation for the lack of durable response to AG120 observed in our models. Indeed, mRNA and protein levels of the IFNγ target CD274 (PD-L1; ref. 62) were increased after AG120 treatment (Supplementary Fig. S8A and S8B). Additionally, mIDH1 inhibition caused accumulation of terminal effector $CD8^+$ T cells, which have a more exhausted phenotype with higher expression of inhibitory checkpoint receptors such as *Pdcd1* (PD-1), *Ctla4*, *Lag3*, and *Havcr2* (Tim3; Supplementary Fig. S4F). Accordingly, we tested whether AG120 has cooperative effects with immune-checkpoint inhibition using anti–PD-1 antibodies to enhance the $CD8^+$ T-cell response to ICC (Supplementary Fig. S8C). However, despite the observed $CD8^+$ T-cell recruitment and PD-L1 induction, this combination did not have a cooperative effect in reducing tumor volume (Supplementary Fig. S8D and S8E). Regulatory T cells (Treg) and other immunosuppressive cells have been implicated in resistance to PD-1 blockade (63) and arise as compensatory mechanisms in highly inflammatory environments. We therefore hypothesized that by promoting IFNγ responsiveness, AG120 could also promote Treg recruitment into the tumors. In this regard, AG120 treatment also increased mRNA levels of a group of cytokines with Treg attractant and activation properties, including *Il16*, *Il6*, *Il1a*, and *Il17d* (Fig. 6A). Correspondingly, we observed enhanced numbers of intratumoral Tregs in tumors evident after six days of treatment (Fig. 6B). Furthermore, there was a significant increase in mRNA and protein expression of the CTLA4 ligand CD80 in the tumor microenvironment (Fig. 6C and D).

Anti-CTLA4 antibody therapy can function as a checkpoint blockade as well as deplete Tregs that express CTLA4 (64) by antibody-dependent cell-mediated cytotoxicity (65), prompting us to assess the efficacy of AG120 plus anti-CTLA4 antibody treatment against mIDH1 ICCs. Tumor-bearing mice were treated with AG120 twice daily and anti-CTLA4 antibody every three days for 26 days. This regimen demonstrated a synergistic antitumor effect compared with either agent alone (Fig. 6E and F; Supplementary Fig. S8F–S8H). Although tumor regressions were not observed upon AG120 treatment (0/10 mice) and were seen in only one of 10 mice administered anti-CTLA4 antibody, nine of 10 mice receiving the combination showed marked tumor regression, including three of 10 with complete responses by the end of the 26-day treatment course. Five mice/group were euthanized for analysis at this time point. Staining of tumor tissue for cleaved caspase-3 revealed pronounced induction of cell death by the AG120 + anti-CTLA4 combination compared with the other treatment conditions (Fig. 6G). Combination treatment also decreased the number of Tregs, which was elevated

Figure 5. Restoration of TET2-dependent antitumor immunity is required for mIDH inhibitor efficacy. **A,** Schematic of IFNγ–TET2 signaling. **B** and **C,** Global levels of 5hmC (measured by ELISA) relative to total input DNA in ICCs from the CKP, CKI^{R132H}, and CKI^{R132C} models (**B**), and CKI^{R132C} ICC allografts (**C**) treated with vehicle or AG120 versus CKP control. Data, mean ± SD. $N = 3$ tumor per group. *, $P < 0.05$; **, $P < 0.01$; ***, $P < 0.001$; unpaired *t* test. **D,** hMeDIP assays with anti-5hmC or IgG antibody were performed in the indicated CRISPR-engineered derivatives of CKI^{R132C} ICC cells grown ± IFNγ and ± AG120 *in vitro*. 5hmC levels on the *Irf1* and *Cd274* promoters were determined by two-step real-time RT-PCR. Data, mean±SD for triplicate experiments. **E,** Relative mRNA expression of *Irf1* and *Cd274* in the indicated CRISPR-engineered derivatives (IDH1wt and mIDH1-sgControl and mIDH1-sg*Tet2-2*) of CKI^{R132C} ICC cells grown ± IFNγ and ± AG120 *in vitro*. mRNA expression was analyzed by two-step real-time RT-PCR. All data were normalized to *Actb* and then to the geometric mean of the vehicle-treated condition. Data, mean ± SD. In the *in vitro* experiments above, AG120 treatment was for three days and IFNγ treatment was for 24 hours. ***, $P < 0.001$; **, $P < 0.01$. **F–I,** Immunocompetent wild-type mice were injected subcutaneously with the indicated derivatives of CKI^{R132C} ICC cells. When tumors reached ~100 mm^3 in volume, animals were randomized into vehicle and AG120 groups. **F,** Analysis of serial changes in tumor volume. $N = 6$ mice per group. Data, means ± SEM. ***, $P < 0.001$; ns, not significant; unpaired *t* test. **G,** IHC staining for cleaved caspase-3 (casp-3) at 15 days of treatment; right, quantification. Data, mean ± SD; ***, $P < 0.001$; unpaired *t* test. **H** and **I,** Heat maps of relative expression of an annotated panel of IFNγ-stimulated genes (**H**) and murine MHC genes (**I**) in magnetic bead–sorted tumor cells from the indicated allograft models treated with AG120 or vehicle for 5 days. The analysis used the nCounter PanCancer mouse immune profiling gene-expression platform (NanoString Technologies). **J** and **K,** CKI^{R132C} ICC cells were CRISPR-engineered with control sgRNA and sg*Ifngr1*. **J,** Detection of IFNGR1, STAT1, phospho-STAT1(Y701), and phospho-STAT1(S727) proteins by immunoblot. β-Actin serves as an internal loading control. **K,** Immunocompetent wild-type mice were injected subcutaneously with the indicated derivatives of CKI^{R132C} ICC cells. When tumors reached ~100 mm^3 in volume, animals were randomized into vehicle and AG120 groups. Analysis of serial changes in tumor volume. $N = 6$ mice per group. Data, means ± SEM. ***, $P < 0.001$; unpaired *t* test. Scale bar, 100 μm (**G**).

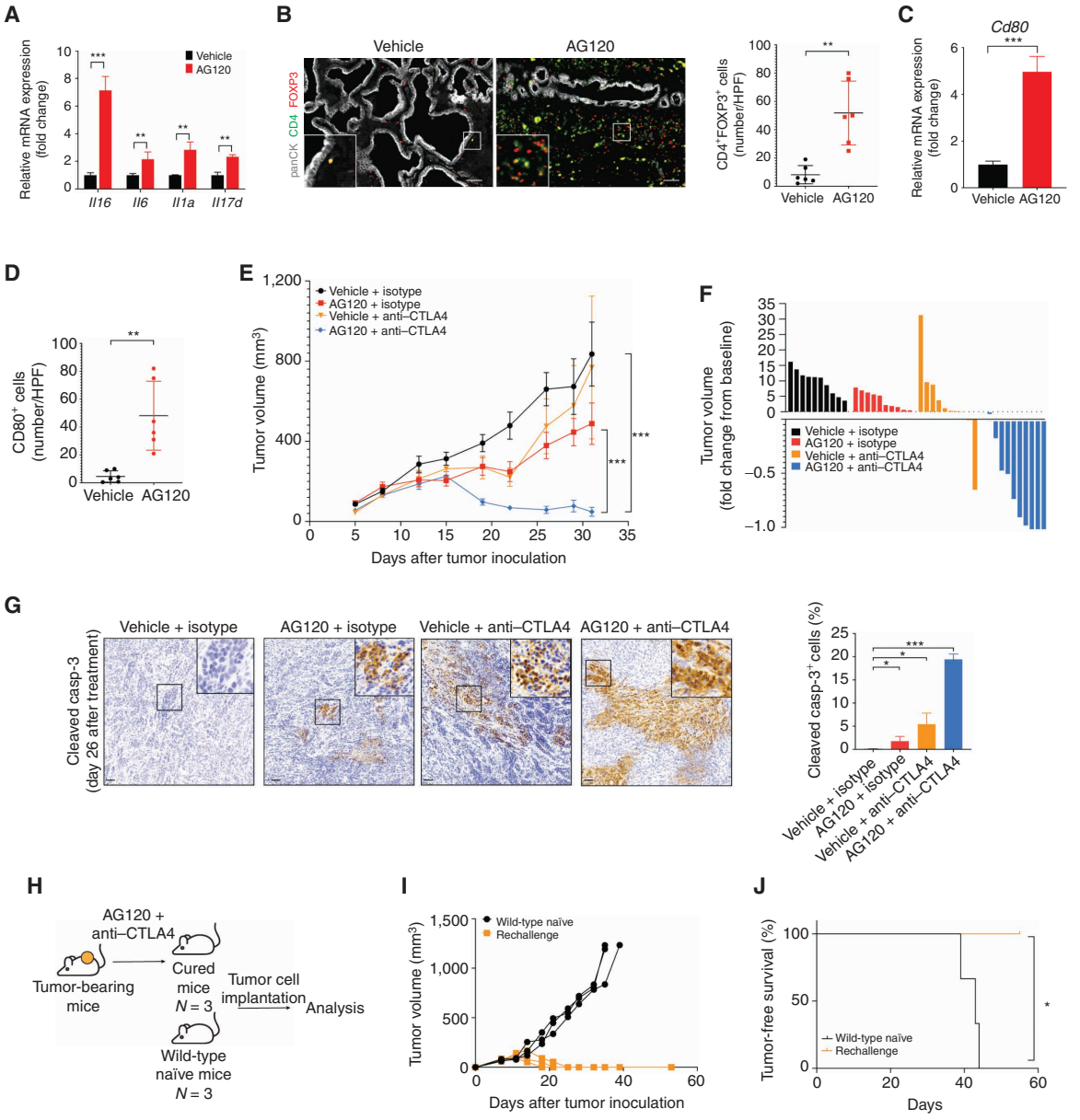

Figure 6. mIDH inhibition stimulates immune checkpoints and Treg recruitment and synergizes with anti-CTLA4 antibody treatment. **A,** Levels of *Il16*, *Il6*, *Il1a*, and *Il17d* mRNA in purified ICC cells from AG120-treated and vehicle-treated CKI^{R132C} allograft tumors. Transcript levels were measured as Fragments Per Kilobase of transcript per Million mapped reads (FPKM) values by RNA-seq analysis. Data, mean±SD. **, $P < 0.01$; ***, $P < 0.001$; unpaired *t* test. **B,** Representative fluorescence-stained sections of ICCs arising in the CKI^{R132C} GEMM upon treatment with vehicle or AG120 for 6 days; green: panCK; red: FOXP3; magenta: CD4; right: quantification. Data, mean±SD. **, $P < 0.01$; unpaired *t* test. **C,** Relative mRNA expression of *Cd80* in vehicle- and AG120-treated bulk tumors by two-step real-time RT-PCR. All data were normalized to *Actb* and then to the geometric mean of vehicle-treated tumors. Data, mean ± SD; ***, $P < 0.001$; unpaired *t* test. **D,** Quantification of IHC-stained sections for CD80 in tumors from vehicle-treated mice and AG120-treated mice. Data, mean ± SD; **, $P < 0.01$; unpaired *t* test. **E** and **F,** Immunocompetent wild-type mice were injected s.c. with CKI^{R132C} ICC cells. When tumors reached ~100 mm^3 in volume, animals were randomized into vehicle + isotype antibody, AG120 + isotype, vehicle + anti-CTLA4 antibody, and AG120 + anti-CTLA4 antibody groups. **E,** Analysis of serial changes in tumor volume. $N = 10$ mice per group. Data, means ± SEM. ***, $P < 0.001$; unpaired *t* test. **F,** Waterfall plot of the maximum percentage change in tumor volume from baseline at day 32 after tumor inoculation (26 days of treatment) in each group. **G,** IHC staining for cleaved caspase-3 (casp-3) in ICC allografts from mice in the indicated treatment groups; right: quantification. Data, mean ± SD; ***, $P < 0.001$; *, $P < 0.05$; unpaired *t* test. **H,** Approach to studying whether combination treatment elicited durable immune memory. **I,** Tumor-naïve immunocompetent wild-type mice and mice cured by the AG120 + anti-CTLA4 therapy 125 days after primary challenge were injected subcutaneously with CKI^{R132C} primary ICC cells and analyzed for serial changes in tumor volume. $N = 3$ mice per group. **J,** Kaplan–Meier analysis for time until tumor progression necessitated euthanasia ($N = 3$; *N*, mouse numbers). Kaplan–Meier curves were analyzed by the log-rank test. *, $P < 0.05$ was considered statistically significant. Scale bars, 100 μm (**B**) and 50 μm (**G**).

by single-agent AG120 treatment (Supplementary Fig. S8G). The remaining animals were monitored long term without treatment to assess the completeness and durability of this response. Strikingly, whereas tumors in the single-agent and vehicle groups all showed rapid progression requiring euthanasia (median, 30–40 days after treatment initiation), three of five mice in the combination group remained tumor-free for >125 days and the other two progressed at 55 and 70 days (Supplementary Fig. S8H and S8I).

To investigate whether combination treatment elicited sustained tumor-specific T-cell responses, mice that were apparently cured by AG120 + anti-CTLA4 therapy (125 days following initial treatment/90 days after cessation of treatment) were rechallenged by injection of CKI^{R132C} ICC cells. Tumor-naïve mice were used as controls. All three cured mice exhibited complete protection from rechallenge, showing no evidence of tumors >50 days after tumor inoculation, compared with naïve animals that displayed the expected rapid tumor development (Fig. 6H–J). Thus, although AG120 treatment results in the simultaneous recruitment of effector and immunoregulatory cells, additional CTLA4 blockade favored the effector response, resulting in an almost complete tumor remission and sustained immunologic memory in this mIDH1 ICC model.

DISCUSSION

Our studies addressed the functions of mutant IDH1 in the sustained growth of an advanced solid malignancy. By developing a mouse model that recapitulates the genetics and histopathologic features of human ICC, we demonstrated that mIDH1 supports ICC tumor maintenance through (R)-2HG–mediated TET2 inactivation and suppression of antitumor immunity. mIDH1 inhibition reverted the immune-evasion phenotype, provoking rapid CD8$^+$ T-cell recruitment and effector function, TET2-dependent epigenetic response to IFNγ in tumor cells, and decreased tumor growth. Although immune-checkpoint activation and Treg stimulation led to eventual tumor progression, dual treatment with anti-CTLA4 antibody conferred complete and durable responses.

The data show that mIDH1 causes insensitivity of ICC cells to immune-derived signals and impaired CD8$^+$ T-cell function through distinct, TET2-dependent and TET2-independent mechanisms. TET2 activity was compromised in our mIDH1 CKI^{R132C} model and in human mIDH1 ICC cells due to high (R)-2HG levels, whereas TET2 function was restored by AG120 treatment. *Tet2*-KO conferred complete resistance to AG120 treatment *in vivo* but did not affect CD8$^+$ T-cell infiltration or IFNγ induction. Rather, TET2-deficient ICC cells failed to induce the IFNγ response program. IFNGR1 ablation also caused mIDH1 tumors to become AG120 insensitive, consistent with IFNγ response serving as the primary growth-inhibitory output of TET2 in this setting. The antitumor effects of IFNγ–TET2 pathway stimulation following mIDH1 inhibition were linked to promotion of tumor cell death, proliferative arrest, and antigen presentation (Fig. 5I; Supplementary Fig. S7F).

mIDH1 inhibition rapidly stimulated CD8$^+$ T-cell infiltration and effector function in the ICC model. Our data support a role for reduction in direct paracrine signaling by (R)-2HG signaling in modulating effector function. mIDH1 tumors secrete high levels of (R)-2HG (Supplementary Fig. S3G, S3J, and S3L). Moreover, CD8$^+$ T cells in our mIDH1 ICC allograft model accumulate significant levels of (R)-2HG (Supplementary Fig. S5A). Exogenous (R)-2HG has been reported to have diverse effects on T-cell function, including suppressing proliferation and activation (18, 66, 67). We show that (R)-2HG treatment of activated CD8$^+$ T cells *in vitro* impairs production of IFNγ and other cytokines, associated with defects in glycolysis and mitochondrial fitness—findings that are in keeping with scRNA-seq analysis of CD8$^+$ TILs revealing increased effector scores and enrichment of these metabolic signatures upon AG120 treatment *in vivo*. These observations complement studies from Bunse and colleagues (18) showing that (R)-2HG suppresses activation of naïve T-cell populations, particularly CD4$^+$ T cells. The defect in lymphocyte recruitment may not only involve direct paracrine effects of (R)-2HG but could also be the result of intrinsic defects in innate immunity of mIDH1 tumor cells. In this regard, we observed that AG120 coordinately downregulated the chemokines CXCL1, CXCL2, and CCL2, which can potently suppress T-cell recruitment. CXCL1 has been shown to be epigenetically activated by H3K4-targeted demethylases (52), which are potential targets of (R)-2HG (3, 8). In addition, our RNA-seq analysis indicates that AG120 induces immunostimulatory type I IFN signaling that can confer an innate immune response (Fig. 2H). Defining the signals that direct the initial recruitment and activation of CD8$^+$ T cells to these formerly immunologically cold tumors will be important in comprehensively explaining how mIDH1 inhibition induces antitumor immunity. More broadly, it will be critical to establish the sequential alterations in tumor biology resulting from mIDH1 inhibition, elucidating the full constellation of cell types in the tumor microenvironment targeted by (R)-2HG or by other tumor-derived factors and deciphering the resulting cross-talk in mIDH1 ICC.

Although the IFNγ response was required for the therapeutic efficacy of mIDH1 inhibitor treatment, sustained IFNγ signaling also likely contributed to the ultimate dampening of antitumor immunity via immune-checkpoint activation. We observed induction of PD-L1 expression in the tumor cells; increased expression of inhibitory checkpoints in CD8$^+$ cells, including *Pdcd1* (PD-1) and *Ctla4* (Supplementary Fig. S4F); and elevation in CD80 in the tumor microenvironment (Fig. 6C and D). AG120 also provoked significant recruitment of Tregs, which, coupled with the ability of PD-1 blockade to activate and expand tumor-infiltrating PD-1$^+$ Tregs (68), may have contributed to the failure of AG120 + PD-1 blockade in our model. Conversely, the dual Treg-depleting and CD8$^+$ T cell–reactivating ability of anti-CTLA4 antibody treatment (69) is consistent with the specific and potent synergy conferred by combined AG120 + CTLA4 blockade (Fig. 6E). In addition to being the ligand for CTLA4, CD80 provides a costimulatory signal to T cells. Because CD80 is expressed primarily by antigen-presenting cells, the increased number of CD80$^+$ cells (Fig. 6D) suggests that AG120 treatment augmented costimulatory capacity in the tumor microenvironment. However, the ability of

CD80 to activate T cells is inhibited by Tregs and CTLA4 on infiltrating CD8$^+$ T cells. In this setting, CTLA4 blockade unleashes the costimulatory capacity of CD80 and promotes T-cell activity (70). Thus, mIDH1 inhibition in patients with ICC and other solid tumor malignancies may enhance the response to immune-checkpoint blockade by restoring tumor-intrinsic sensitivity to IFNγ.

In patients with AML and immunodeficient xenograft models of the disease, mIDH inhibition promotes maturation of leukemic stem cells to terminally differentiated myeloid cells—which have a short lifespan like their normal equivalents—leading to frequent complete remissions (26). This central role of induction of differentiation in the therapeutic efficacy of mIDH inhibition is in keeping with the established treatment paradigm of differentiation therapy in hematopoietic malignancies. In solid tumors, there is no clear precedent for differentiation-based treatments. Nevertheless, strong induction of hepatocyte lineage genes was observed in on-treatment versus pretreatment biopsies from the ivosidenib trial in mIDH1 ICC, correlating with improved patient outcomes (70) and consistent with prior observations linking mIDH1 to a block in hepatocyte differentiation (23). Although mIDH1 inhibition stimulated comparable hepatocyte signatures in our mouse ICC model, we found that these features of apparent differentiation could be uncoupled from therapeutic response; they were also stimulated by AG120 in the context of *Tet2*-KO, despite the lack of antitumor efficacy observed in this setting. Indeed, in the liver, where mature hepatocyte cells have long lifespan and retain high proliferative capacity, differentiation itself would not be expected to have analogous antitumor effects to those observed in hematopoietic malignancies. It remains possible that—although not sufficient—this hepatocyte differentiation program is indeed necessary for AG120 response. In this regard, hepatocytes possess intrinsic antiviral mechanisms that increase sensitivity to inflammatory cytokines (71, 72), and, more generally, switches in cell lineage identity and associated cell-surface antigens have been shown to increase CD8$^+$ T-cell antitumor immunity (73).

As for most genetic subsets of the disease, patients with mIDH1 ICC have poor outcomes upon treatment with current standard-of-care chemotherapy or immune-checkpoint blockade. Divergent molecularly targeted therapeutic strategies are currently being explored preclinically and clinically for these tumors. The uncertain contributions of mIDH1 to tumor maintenance have prompted multiple studies aimed at identifying synthetic lethal therapeutic interactions with mIDH as a treatment approach rather than inhibiting the mutant enzyme (11, 14, 40–43). On the other hand, mIDH itself is a particularly attractive target on which to base therapeutic strategies because of the very high specificity of mIDH inhibitors for the mutant tumor cells and consequent low systemic toxicity (32, 34). Indeed, the increased progression-free survival conferred by ivosidenib/AG120 in the phase III trial for mIDH1 ICC is an encouraging clinical advance, although the modest objective response rate highlights the need to understand the biological roles of mutant IDH in the ongoing growth of these tumors to inform further clinical development. Our studies in an aggressive ICC model reveal mechanisms by which mIDH1 supports tumor maintenance and show that inhibition of the mutant enzyme engenders sensitivity to immunotherapy.

In summary, we conclude that mIDH1 functions as an atypical oncogene in this model of advanced ICC, whose inhibition suppresses tumor growth in a manner that is fully dependent on intact immune function. The restoration of T-cell immunity via the IFNγ–TET2 axis following mIDH1 inhibition and the preclinical efficacy of combined CTLA4 blockade provide a rational foundation for advancing immunotherapy in the treatment of mIDH1 ICC.

METHODS

Resource Availability

Lead Contact. Further information and requests for resources and reagents should be directed to and will be fulfilled by the lead contact, Nabeel Bardeesy (bardeesy.nabeel@mgh.harvard.edu).

Materials Availability. Mouse lines generated in this study may be available upon request. This study did not generate new unique reagents. All other relevant data are available upon request.

Data and Code Availability. Sorted tumor RNA-seq data have been deposited in the ArrayExpress database at EMBL-EBI (www.ebi.ac.uk/arrayexpress) under accession number E-MTAB-11112. 10x scRNA-seq data that support the findings of this study have been deposited in the Gene Expression Omnibus database under accession number GSE173612. NanoString data are in Supplementary Table S2.

Experimental Model and Subject Details

Mice. Mice were housed in pathogen-free animal facilities. All experiments were approved by the Massachusetts General Hospital (MGH) Institutional Animal Care and Use Committee (IACUC; protocols 2005N000148 and 2019N000116).

Mouse strains including 129SF1 (#101043, RRID: IMSR_JAX:101043), C57Bl/6 (#000664, RRID: IMSR_JAX:000664), B6.Cg-Speer6-ps1$^{Tg(Alb\text{-}cre)21Mgn}$ (#003574, RRID: IMSR_JAX:003574), and NOD.CB17-Prkdc^{scid}Il2rg^{tm1Wjl} (#005557; RRID: IMSR_JAX:005557) were obtained from The Jackson Laboratory. LSL-Kras^{G12D} (The Jackson Laboratory, #008179, RRID: IMSR_JAX: 008179) mice were kindly provided by D. Tuveson and T. Jacks. Mice were maintained on a mixed 129SF1/C57Bl/6 background and cross-bred at Mendelian frequency to generate the *Alb-Cre* (C), *Cre-Kras* (CK), *Cre-Kras-IDH1*^{R132H} (CKI^{R132H}), and *Cre-Kras-IDH1*^{R132C} (CKI^{R132C}) genotypes. Data presented include both male and female mice. Wild-type mice from littermate or B6129SF1/J (JAX #101043) used for subcutaneous and orthotopic injection were between ages 6 and 8 weeks at the time of implantation. Experimental groups were matched for age and sex. All experiments were carried out according to institutional guidelines at MGH. Mouse genotypes were monitored with routine genotyping of each litter and bred selectively in line with IACUC-prescribed protocols.

Human Samples. Patient biopsy samples were collected and analyzed after written informed consent to the institutional tissue collection protocol, and approval by the MGH Institutional Review Board and Internal Review Board of the Dana-Farber/Harvard Cancer Center (DFCI Protocol Nos. 19-699, 14-046, and 13-416)–approved protocol and in accordance with the declaration of Helsinki.

Cell Lines. Murine IDH1^{R132C} ICC cell lines 2205 (male), 2275-4 (female), and 4411 (female) were derived from B6/129SF1 background CKI^{R132C} ICC mice. The murine ICC IDH1^{R132H} cell line R132H was derived from a B6/129SF1 background CKI^{R132H} ICC

mouse. Murine ICC IDH1wt cell lines 158 (male), 215 (female), and 254 (male) were derived from B6/129SF1 background CKP mice. ICC cell lines were validated by RT-qPCR (see Supplementary Fig. S3A). The JF001 murine HCC cell line used for comparative mRNA expression was derived from a Mst1/Mst2 KO GEMM (74). All of the above cell lines were cultured in RPMI 1640 (+) L-glutamine, 25 mmol/L HEPES (Corning, catalog no. 10-041-CV) containing 10% FBS (GIBCO, catalog no. 11995040) and 1% penicillin–streptomycin (PS; GIBCO, catalog no. 15140122). HEK293T cells used for packaging lentivirus were cultured in DMEM (GIBCO, catalog no. 11995040) containing 10% FBS (GIBCO, catalog no. 11995040) and 1% PS (GIBCO, catalog no. 15140122). All cells were cultured using standard procedures in a 37°C humidified incubator with 5% CO_2. Cells were tested routinely for *Mycoplasma* using the PCR-based Venor GeM Mycoplasma Detection Kit (Sigma-Aldrich).

Detailed Methods

Generation of the Latent LSL-Idh1^{R132H} Knock-in Mouse Strain. To construct the latent LSL-Idh1^{R132H} knock-in allele, the Idh1-containing locus was cloned from a bacterial artificial chromosome library. The targeting vector was generated by inserting a floxed STOP cassette (Lox-STOP-Lox) into the mouse genomic Idh1 locus upstream of a modified exon 3 engineered to contain a G → A transition in codon 132. The construct was then electroporated into 129S6 embryonic stem cells. Targeted cells were selected by standard techniques and verified by Southern blot analysis. Blastocyst injections were carried out with three different targeted clones, and transmitting chimeric mice were bred to generate the LSL-Idh1^{R132H} allele.

Generation of the Latent Idh1^{R132H} Knock-in Mouse Strain. To generate the latent IDH1^{R132C} knock-in mouse strain, CRISPR–Cas9-mediated genome engineering in zygotes (75) was performed at the Harvard University Genome Modification Facility. In brief, LSL-Idh1^{R132H} zygotes were subject to piezo-driven cytoplasmic injection of single-stranded IDH1^{R132C} DNA donor, Cas9 protein (PNA Bio), and *in vitro*–transcribed and *in vitro*–purified sgRNAs against the IDH1^{R132H} locus. Following embryo transfer, offspring were genotyped by sequencing 800 bp surrounding the Idh1^{R132H} genomic locus. Multiple founders with the desired conversion of the LSL-IDH1^{R132H} allele to the LSL-IDH1^{R132C} allele were bred to the Albumin-Cre mouse strain, and progeny for each founder were tested for (R)-2HG production in the liver. Four sequence- and (R)-2HG–validated founder lines were selected for further experimental study. Offspring were successively crossed with LSL-KRAS^{G12D} mice.

Histologic Characterization of the GEMM. The following compound mutant mouse strains were studied for liver cancer and associated phenotypes: C (*Alb-Cre*), CI^{R132C} (*Alb-Cre*; *Idh1*^{R132C}), CI^{R132H} (*Alb-Cre*; *Idh1*^{R132H}), CK (*Alb-Cre*; *Kras*^{G12D}), CKI^{R132H} (*Alb-Cre*; *Kras*^{G12D}; *Idh1*^{R132H}), and CKI^{R132C} (*Alb-Cre*; *Kras*^{G12D}; *Idh1*^{R132C}) cohorts. All experiments were performed on >85% C57/Bl/6 background. Hematoxylin and eosin staining was performed by iHisto (iHisto.io). Formalin-fixed tumor samples were processed, embedded in paraffin, sectioned at 4 μm, and stained with hematoxylin and eosin. Histologic characterization was performed in a manner blinded to genotype by an experienced gastrointestinal cancer pathologist (V. Deshpande). The histologic classification of each primary tumor and metastatic tumors reported in Supplementary Fig. S1F and S1G was determined by evaluation of cross-sectional slides from two axes. ICC was identified by morphologic examination and validated by CK19 staining. For the cumulative analysis in Supplementary Fig. S1G, the histologic type representing the largest cross-sectional area (ICC or HCC) of each tumor-bearing mouse was reported, as was the presence of each histologic type in any proportion. Most CK, CI^{R132C}, and CI^{R132H} mice did not develop tumors, and those that did all exhibited HCC features as the predominant malignant phenotype with minor presence of ICC or undifferentiated tumor fractions. CKI^{R132H} mice exhibited intermediate features with a phenotype dominated by HCC with undifferentiated tumor fractions and with very rare presence of frank ICC. CKI^{R132C} mice exhibited a phenotype dominated by ICC, and some mice developed the mixture presentation of ICC and HCC.

Survival Analysis. Groups were assigned based on regular genotyping of each litter and included both male and female mice. All mice included in the survival analysis were euthanized when criteria for disease burden were reached (including abdominal distension that impeded movement, loss of >15% of body weight, labored breathing, and/or abnormal posture). Overall survival refers to all mice that were euthanized based on poor body condition and includes tumors and other causes of morbidity (e.g., hepatomegaly). Tumor-free survival refers to the age of mice that were euthanized based on poor body condition and were found to have liver tumors as the primary morbidity. Additionally, ICC-free survival was monitored and recorded when mice meet criteria for disease burden with tumors dominated by ICC. Kaplan–Meier estimators of survival were used to visualize the survival curves. Significant differences between groups were determined by the log-rank test ($P < 0.001$).

Tumor Dissociation, Cell Isolation, and Sorting. Mice were euthanized and tumors were dissected, then rinsed in ice-cold PBS (GIBCO) + 3% FBS (GIBCO) and cut into <3 mm pieces with surgical scissors. Tumor fragments were then dissociated to single-cell suspensions using the Miltenyi Mouse Tumor Dissociation Kit (Miltenyi, catalog no. 130-096-730, RRID:SCR_020285) and gentleMacs Octo-Dissociator (Miltenyi, #130–095–937) on program 37C_m_TDK_2 as described by the manufacturer's protocols. Following dissociation, reactions were quenched with 10 mL of ice-cold RPMI 1640 (Corning) + 1%FBS (GIBCO) and strained through a 70-μm filter. In order to separate tumor cells from stromal cells or to isolate tumor-infiltrating CD8$^+$ T cells, the filtrate was then incubated with the Nontumor Cell Depletion Cocktail (Miltenyi, catalog no. 130-110-187) or CD8 (TIL) MicroBeads for mouse (Miltenyi, catalog no. 130-116-478) for 15 minutes at 4°C, respectively. The samples were then magnetically separated by elution through a Miltenyi LS column (Miltenyi, catalog no. 130-042-401) that was mounted on a MacsMultistand (Miltenyi, #130-042-303) as described by the manufacturer's protocols. The isolated tumor cells were centrifuged at 1,200 rpm for 5 minutes at 4°C and processed for further application or stored at –80°C.

Generation of Cell Lines. Mice exhibiting poor body condition or abdominal distension were euthanized in accordance with guidelines established by our institution's IACUC. Upon necropsy, tumors were processed as described in "Tumor Dissociation, Cell Isolation, and Sorting." Cell pellet was resuspended in DMEM + 1% FBS before the cell suspension was spun down once more. Cells were then resuspended in RPMI 1640 containing 25 mmol/L HEPES and 100 μg/mL L-glutamine (CORNING) supplemented with 10% FBS (GIBCO) and 1% PS and seeded at a density of >3 × 10^6 cells on a 6-cm collagen-coated plate. Cells were passaged at least five times until they were free of all fibroblasts. Cells were detached from the plate using 0.25% Trypsin-EDTA (GIBCO). IDH1-mutant cell lines were validated by confirmation of elevated 2HG levels via mass spectrometry and by qRT-PCR analysis of ICC markers.

Immunoblotting. Tumor samples for immunoblotting were thawed and suspended in Invitrogen lysis buffer (Invitrogen) supplemented with Pierce Halt Protease and Phosphatase Inhibitor Cocktail (Thermo Fisher). Tumor fragments were mechanically homogenized using a Precellys 24 Tissue Homogenizer (Bertin Instruments) and

2.8-mm disruptor beads (Bertin Instruments). Cell line samples for Western blot analysis were lysed in similarly prepared Invitrogen lysis RIPA buffer. Lysates were then sonicated on ice for six minutes with a Bioruptor UCD-200 (Diagenode) and centrifuged. Total protein amounts were measured with the Pierce BCA Protein Assay (Thermo Fisher), and sample concentrations were normalized with a lysis buffer. Samples were run on Tris-Glycine SDS polyacrylamide gels and transferred to PVDF membranes. Membranes were incubated overnight at 4°C with antibodies to Stat1 (Cell Signaling Technology, catalog no. 9172; RRID:AB_2198300, 1:1,000), phospho-Stat1 (Y701; Cell Signaling Technology, catalog no. 5375, RRID:AB_10860071, 1:1,000), phospho-Stat1 (S727; Cell Signaling Technology, catalog no. 8826; RRID:AB_2773718; 1:1,000), β-actin (Sigma-Aldrich, catalog no. A5316; clone: AC-74; RRID:AB_476743; 1:10,000), and GAPDH (Thermo Fisher Scientific, catalog no. AM4300, RRID:AB_2536381; 1:10,000) suspended in 1× TBS-T with 5% (w/v) BSA (Thermo Fisher Scientific). After washing, membranes were then incubated with corresponding horseradish peroxidase–coupled secondary antibodies for one hour at room temperature (RT) on a platform shaker. Primary antibody binding was detected using an enhanced chemiluminescent substrate and imaged with a Bio-Rad ChemiDoc Imaging System (Bio-Rad).

***mIDH1 Cell Viability upon AG120 Treatment* In Vitro.** The $IDH1^{R132C}$ cell lines, 2275–4, 4411, and 2205, were cultured in RPMI 1640 containing 25 mmol/L HEPES and 100 μg/mL L-glutamine (CORNING) supplemented with 10% FBS (GIBCO) and 1% PS (GIBCO) and seeded in triplicate onto a white clear-bottomed 96-well plate at a density of 1×10^4 cells per well. Cells were treated with either 1 μmol/L AG120 or DMSO for a period of five days. On day 5 of treatment, cell viability was measured using the CellTiter-Glo Luminescent Cell Viability Assay (Promega, catalog no. G7573) in accordance with manufacturer-recommended protocols.

***IHC Staining*.** IHC staining was performed by iHisto (iHisto.io). Samples were processed, embedded in paraffin, and sectioned at 4 μm. Paraffin sections were then deparaffinized and hydrated using the following steps: 15 minutes in xylene twice; 5, 5, and 5 minutes in 100%, 100%, and 75% ethanol, respectively; and 5 minutes in PBS at RT repeated three times. Antigen retrieval was achieved by boiling the sections in 10 mmol/L sodium citrate for 10 minutes in a microwave oven and 5 minutes of cooling at RT. Sections were then washed with PBS three times, and treated with 3% H_2O_2 for 15 minutes and 5% BSA for 20 minutes. The sections were incubated with primary antibodies rabbit anti-CD8 (Cell Signaling Technology, catalog no. 98941, RRID:AB_2756376; 1:400) overnight at 4°C. Subsequently, the sections were immunohistochemically stained with HRP-conjugated goat anti-rabbit secondary antibodies (Thermo Fisher Scientific, catalog no. G-21234, RRID: AB_2536530; 1:2,000) for 50 minutes at RT. After incubation with the DAB Kit (Thermo Scientific), whole slide scanning (40×) was performed on an EasyScan infinity (Motic).

Multiplex Immunofluorescence Staining (Normal). Immunofluorescence staining was performed by iHisto (iHisto.io). Samples were processed, embedded in paraffin, and sectioned at 4 μm. Paraffin sections were then deparaffinized and hydrated using the following steps: 15 minutes in xylene twice; 5, 5, and 5 minutes in 100%, 100%, and 75% ethanol, respectively; and 5 minutes in PBS at RT repeated three times. Antigen retrieval was achieved by boiling the sections in 10 mmol/L sodium citrate for 10 minutes in a microwave oven and 5 minutes of cooling at RT. Sections were then washed with PBS three times, and treated with 3% H_2O_2 for 15 minutes and 5% BSA for 20 minutes. The sections were incubated with rabbit anti–Ki-67 (Servicebio, catalog no. GB13030-2; 1:500) and mouse anti-panCK (Novus Biologicals, catalog no. NBP-29429; 1:200) overnight at 4°C. Subsequently, the sections were immunohistochemically stained with CY3-conjugated goat anti-rabbit (#A10520, Invitrogen, 1:2,000) and FITC-conjugated goat anti-mouse (FITC; Thermo Fisher Scientific, catalog no. A10520, RRID:AB_2534029) for 50 minutes at RT. After incubation with DAPI, whole slide scanning (40×) was performed on a Panoramic midi scanner (3DHistech).

Multiplex Immunofluorescence Staining (TSA). Immunofluorescence staining was performed by iHisto (ihisto.io). Samples were processed, embedded in paraffin, and sectioned at 4 μm. Paraffin sections were then deparaffinized and hydrated using the following steps: 15 minutes in xylene twice; 5, 5, and 5 minutes in 100%, 100%, and 75% ethanol, respectively; and 5 minutes in PBS at RT repeated three times. Antigen retrieval was achieved by boiling the sections in 10 mmol/L sodium citrate for 10 minutes in a microwave oven and 5 minutes of cooling at RT. Sections were then washed with PBS three times, and treated with 3% H_2O_2 for 15 minutes and 5% BSA for 20 minutes. The sections were incubated with the primary antibody rabbit Anti-Foxp3 (Cell Signaling Technology, catalog no. 12653, RRID: AB_2797979; 1:1,000) overnight at 4°C. Sections were rinsed with PBS and incubated with secondary antibody HRP-conjugated goat anti-rabbit secondary antibodies (Thermo Fisher Scientific, catalog no. G-21234, RRID:AB_2536530; 1:2,000) for 50 minutes at RT. After rinsing with PBS, sections were incubated for 10 minutes at RT in Alexa Fluor 555 Tyramide Reagent (Thermo Fisher Scientific, catalog no. B40955). Antigen retrieval was achieved by boiling the sections in 10 mmol/L sodium citrate for 10 minutes in a microwave oven and 5 minutes of cooling at RT. Sections were then washed with PBS three times, and treated with 3% H_2O_2 for 15 minutes and 5% BSA for 20 minutes. The sections were incubated with rabbit anti-CD4 (Cell Signaling Technology, catalog no. 25229, RRID:AB_2798898; 1:500) and mouse anti-panCK (Novus Biologicals, catalog no. NBP-29429; 1:200) overnight at 4°C. Subsequently, the sections were immunohistochemically stained with CY5-conjugated goat anti-rabbit (Thermo Fisher Scientific, catalog no. A-21245, RRID:AB_2535813; 1:2,000) and FITC-conjugated goat anti-mouse (Thermo Fisher Scientific, cat. #A16073, RRID:AB_2534746; 1:2,000) for 50 minutes at RT. After incubation with DAPI, whole slide scanning (40×) was performed on a Panoramic midi scanner (3DHistech).

In Vitro *T-cell Isolation and Stimulation*. In order to isolate murine T cells, healthy B6129SF1 (The Jackson Laboratory, #101043, RRID: IMSR_JAX:101043) mice, ages 6- to 12-weeks, were euthanized, and their spleens were collected. Using antiseptic technique, spleens were then placed on a 70-μm cell strainer (Fisher Scientific) and ground down with a rubber plunger. The cell filtrate was collected in a 50-mL conical tube and spun down (350 × *g*, 5 minutes, RT). The supernatant was gently decanted, and the pellet was resuspended in 5 mL of ACK Red Blood Cell Lysis Buffer (GIBCO) and incubated for 5 minutes at RT. The solution was quenched with 45 mL of PBS and centrifuged (350 × *g*, 5 minutes, RT). The supernatant was aspirated, and the pellet was resuspended in 10 mL of sterile MACS buffer (PBS, 0.5% BSA w/v). The live cells were counted using a glass hemocytometer before being centrifuged again (350 × *g*, 5 minutes, RT). The pellet was resuspended in 40 μL of MACS buffer per 10 million cells and transferred to a microcentrifuge tube. Using the naïve $CD8^+$ T-cell Isolation Kit (Miltenyi Biotec, catalog no. 130-096-543) according to the manufacturer's protocols, nontarget cells were magnetically labeled. The cell suspension was then passed through a Miltenyi LS column mounted on a MACS Multistand (Miltenyi), and $CD8^+$ T cells were collected in the flow-through. The filtrate was spun down (350 × *g*, 5 minutes, RT), and the cells were counted using a hemocytometer. Adjusting the concentration to 1 million cells/mL with RPMI 1640, IL2 (BioLegend, catalog no. 575404) was added to a final concentration of 100 U/mL, 2 μmol/L 2-ME (Sigma-Aldrich) and Dynabeads Mouse T-Activator CD3/CD28 beads

(1:4 ratio; Thermo Fisher Scientific, catalog no. 11456D) was added to the culture. The cells were plated at 1 million cells per well and placed in the incubator for two days. On day 3, once it was evident that the cells were healthy and proliferating, the cells were collected, and the anti-CD3/CD28 antibody–coated magnetic beads were removed. The cells were centrifuged (350 ×*g*, 5 minutes, RT) and counted while maintaining continuous IL2 stimulation. Cells were expanded and kept in a resting state by plating at 1 million cells per milliliter on appropriate culture plates.

Mitochondrial Respiration and Glycolysis Measurement. Mitochondrial respiration and glycolysis were measured by oxygen consumption and ECAR, respectively, using the XF Cell Mito Stress Test Kit (Seahorse Bioscience). After pretreatment with (R)-2HG and stimulation with anti-CD3– and anti-CD28–coated beads (1:4), 500,000 resting $CD8^+$ T cells per well were seeded on poly-D-lysine–coated Seahorse XF96 Cell Culture Microplate in RPMI 1640 Base Medium (US Biological, R9011, pH 7.4) supplemented with 10 mmol/L glucose, 2 mmol/L glutamine, and 1 mmol/L sodium pyruvate (all Sigma-Aldrich). Assays were performed using the XF Cell Mito Stress Test Kit (Seahorse Bioscience) according to the manufacturer's instructions using 1.5 μmol/L oligomycin to inhibit ATP synthase, 1 μmol/L FCCP to uncouple oxygen consumption from ATP production, and 0.5 μmol/L rotenone/antimycin A to stop electron transport chain, on an XFe96 analyzer (Seahorse Bioscience). Data were analyzed with Wave software (Seahorse Bioscience) and plotted after export into Microsoft Excel.

Detection of Global 5hmC Levels by DNA Dot Blot Assay. Genomic DNA was denatured in 0.1 mol/L NaOH and 10 mmol/L EDTA at 95°C for 10 minutes, and then neutralized by adding an equal volume of 20× saline sodium citrate buffer and immediately chilled on ice. Next, the denatured DNA samples (along with the 2-fold diluted sample: 500, 250, 125, and 62.5 ng) were spotted on an Amersham Hybond N^+ membrane (GE Healthcare) by Bio-Dot (Bio-Rad). Then, the membrane was washed with 3× SCC twice and air-dried for 20 minutes on Whitman paper. The membrane was then UV cross-linked and blocked with Blocking Solution 5% milk and PBST (1 × PBS + 0.1%Tween-20) overnight at 4°C. After blocking, the membrane was incubated with polyclonal 5hmC antibody (Active Motif, #39769, RRID: AB_10013602; 1:5,000) and HRP-conjugated secondary antibody (Vector Laboratories, #PI-1000-1, RRID: AB_2313606; 1:5,000) and then visualized by SuperSignal West Dura Chemiluminescent Substrate (Thermo Scientific, catalog no. 34075).

In Vitro *Methylated DNA Immunoprecipitation.* The 2205 $TET2^+$ and 2205 TET2− cells were cultured in RPMI 1640 (+) L-glutamine, 25 mmol/L HEPES (CORNING), and 10% FBS (GIBCO) + 1% PS (GIBCO) and treated with either 1 μmol/L AG120 or 10 μL DMSO for five days. On the fourth day of treatment, samples were administered either 50 ng/μL murine IFNγ or 10 μL DMSO and incubated for 24 hours at 37°C. Cells were washed with D-PBS, scraped, collected, and centrifuged for 5 minutes at 1,200 rpm before being stored overnight at −80°C. DNA was extracted from cell pellets using the Zymo Research Quick-DNA Miniprep Kit as described by the manufacturer. Genomic DNA (15 μg) from each sample was then sheared to ~400 bp fragments using a Bioruptor UCD-200 (Diagenode) at high power for three 15-minute cycles running at 30-second on/off increments. Shearing of genomic DNA to 300 to 500 bp–sized fragments was confirmed by electrophoresis on a 1.5% agarose gel followed by UV transillumination. Immunoprecipitation was conducted using the Active Motif MeDIP Kit (Active Motif, catalog no. 55009) as described by the manufacturer. Following immunoprecipitation, the DNA was purified using the Qiaquick PCR Purification Kit (Qiagen, catalog no. 28014) according to the manufacturer-supplied protocol. Purified sheared DNA was used for downstream qPCR analysis.

RNA Extraction, Reverse Transcription, and RT-qPCR. Single-cell suspensions from dissociated tumors and cells cultured in a monolayer were homogenized in 300 to 600 μL of TRIzol. RNA was extracted from homogenized samples using the Direct-zol RNA Miniprep Plus Kit (Zymo Research, catalog no. R2072) in accordance with the manufacturer-prescribed protocol. Total RNA was quantified and assessed for quality using a NanoDrop spectrophotometer (Thermo Fisher). Subsequently, 1,000 ng of RNA from each sample was converted to cDNA using the Quantitect Reverse Transcription kit (Qiagen, catalog no. 205311) as directed by the manufacturer. cDNA as well as genomic DNA isolated by immunoprecipitation were quantitatively amplified using Universal SYBR Green (Bio-Rad). Samples were processed using a CFX384 Touch Real-Time PCR Detection System (Bio-Rad), and relative mRNA expression was normalized to *Actb* or *Gapdh* controls. Primers targeting genes associated with biliary differentiation were custom-selected from overlapping lists of trademark hepatic and biliary genes as described by Aizarani and colleagues and MacParland and colleagues (76, 77). Primer sequences are listed in Supplementary Table S3.

NanoString nCounter Immune Profiling. Total RNA was extracted as described above. RNA concentrations were quantified and evaluated for purity using a NanoDrop spectrophotometer (Thermo Fisher, catalog no. ND-ONE-W). For immune profiling, we utilized NanoString's 770-gene Mouse nCounter PanCancer Immune Profiling Panel. Reporter codesets were thawed at RT and subsequently mixed with 70 μL of hybridization buffer to form a master mix. From this master mix, 8 μL was aliquoted into PCR tubes. RNA samples were normalized to 10 ng/μL, and 5 μL from each sample was added into the PCR tubes. Next, 2 μL of Capture probeset was added to each tube. The reaction mixture was then gently mixed, spun down, and loaded into a prewarmed 65°C thermocycler with a heated lid set to 70°C. Samples were allowed to hybridize for 16 to 20 hours, after which they were immediately placed on ice. At this time, a SPRINT cartridge was thawed and allowed to equilibrate to RT. Samples were then individually loaded into the cartridge and inserted into the NanoString nCounter SPRINT Profiler machine (NanoString nCounter Analysis System, RRID:SCR_021712). Raw data were analyzed using NanoString nSolver 4.0. mRNA counts were processed to account for hybridization efficiency, background noise, and sample content and were normalized using the geometric mean of housekeeping genes.

RNA-seq of Sorted Tumor Cells. Tumors were processed as described in "Tumor Dissociation, Cell Isolation, and Sorting." RNA was extracted as described above in accordance with the manufacturer-prescribed protocol. Total RNA was quantified and assessed for quality using a NanoDropTM spectrophotometer (Thermo Fisher). We used the NEBNext Ultra Directional RNA Library Prep Kit for Illumina for RNA-seq library preparation by following the manufacturer's recommendations (NEB). Briefly, mRNA was first enriched with NEBNext rRNA Depletion Kit v2 (Human/Mouse/Rat) with RNA Sample Purification Beads. Enriched mRNAs were fragmented for 15 minutes at 94°C. First-strand and second-strand cDNAs were subsequently synthesized. cDNA fragments were end-repaired and adenylated at the 3′ ends, and universal adapter was ligated to cDNA fragments, followed by index addition and library enrichment with limited-cycle PCR. Sequencing libraries were validated using a DNA chip on the Agilent 2100 Bioanalyzer (Agilent Technologies) and quantified using Qubit 2.0 Fluorometer (Thermo Fisher Scientific–Invitrogen). The constructed library was submitted to GENEWIZ. Total RNA was sequenced on Illumina HiSeq 3000 (2 × 150, paired end) and aligned to the mouse mm10 reference genome using TopHat. The gene-expression values (Fragments Per Kilobase of transcript per Million mapped reads, FPKM) were calculated with Cufflinks, and significant changes in transcript expression were determined with Cuffdiff. After extraction of gene hit counts, the gene hit count table was used for downstream differential expression

analysis. Using DESeq2, a comparison of gene expression between the groups of samples was performed. The Wald test was used to generate *P* values and $\log_2$ fold changes. Genes with adjusted *P* values less than 0.05 and absolute $\log_2$ fold changes greater than 1 were called as differentially expressed genes for each comparison.

scRNA-seq of Tumor-Infiltrating Immune Cells. Eight mice were orthotopically implanted with 10^6 CKI^{R132C} ICC cells. The tumors were allowed seven days to develop masses and were administered an AG120 treatment regimen for six days. Tumors were dissected from mice on day 13 after inoculation and disassociated using the Miltenyi Mouse Tumor Dissociation Kit and gentleMACS Octo-Dissociator (Miltenyi) as per the manufacturer's instructions. After filtering through a 70-mm filter, live cells were isolated using a gradient with Lympholyte-M separation media (Fisher Scientific) as per the manufacturer's instructions. TILs were enriched by $CD45^+$ MACS-positive selection (Miltenyi Biotec, catalog no. 130-052-301). Four representative samples each of vehicle-treated and AG120-treated tumors were selected, and droplet-based isolation of single cells was performed with the Chromium Controller (10x Genomics). Subsequent generation of 5′ sequencing libraries was performed as per manufacturer's instructions (10x Genomics). Characterization of the sequencing library was performed with TapeStation (Agilent) and Qubit (Thermo Fisher) instruments.

Pooled equimolar 5′ 10× output libraries were sequenced using an Illumina SP flow cell using paired-end 91-bp reads, and downstream preprocessing steps were performed using cellranger version 3.0.1. Individual replicate quality was evaluated based on the number of cells recovered, mean reads per cell, and median genes per cell. Early quality control (QC) metrics determined no replicates should be excluded. After initial processing, 43,359 cells were recovered across conditions. Additional cell filtering and downstream analysis were performed using Scanpy version 1.7 (78) to evaluate the number of genes recovered per cell and the percentage of mitochondrial genes. Cells with more than 2,500 genes were excluded as suspected doublets, whereas cells that had fewer than 500 genes were excluded due to poor gene capture. Cells with greater than 10% mitochondrial gene content were excluded. The resulting filtering left 39,810 immune cells. In addition, genes that were not recovered in any cell were also excluded from the downstream analysis.

Gene counts per cell were normalized so that every cell had the same total gene count after normalization. The resulting gene count matrix was then $\log(1 + p)$-transformed, where p is the gene transcript count. Principal component analysis (PCA) and nearest-neighborhood graphs were calculated in order to visualize on a uniform manifold approximation and projection. Harmony was then used to correct PCA embeddings for technical batch effects between replicates (79). Cells were then grouped into 19 distinct clusters using the leiden algorithm. Cell-type classification and labeling were done by calculating differentially expressed marker genes, which can be found in Supplementary Table S4. To gain more granularity between the T- and NK-cell subtypes, subclustering was performed on cells in clusters expressing *Cd8a*, *Cd4*, and *Ncr1* transcripts. New PCA embeddings, nearest-neighborhood graphs, and harmony batch corrections were calculated for this subgroup on a set of 10,000 highly variable genes.

Gene set scoring was performed by using the average expression of genes in a given gene set and subtracting from a reference set of genes. Differentially expressed genes between treatment conditions were calculated using a logistic regression model (80). Ranked lists of differential genes were created using signed *P* values calculated by the logistic regression model and passed to GSEA Prerank to search for enriched gene sets by treatment (81, 82).

Quantitative Flow Cytometry Tumor–Immune Profiling. Cells were stained either with a panel of lymphocyte-associated antibodies against CD8a (BioLegend, catalog no. 100705; clone: 53-6.7 RRID:AB_312744; 1:100), CD4 (BioLegend, catalog no. 116023; clone: RM4-4; RRID:AB_2800579; 1:100), CD45 (BioLegend, catalog no. 103155; clone: 30-F11; RRID:AB_2650656; 1:200), LIVE/DEAD (Thermo Fisher Scientific, catalog no. L34957; 1:1,000), granzyme B (BioLegend, catalog no. 515403; clone: GB11; RRID:AB_2114575; 1:100), IFNγ (BioLegend, catalog no. 505808; clone: XMG1.2; RRID:AB_315402; 1:100), TNFα (BioLegend, catalog no. 506321; clone: MP6-XT22; RRID:AB_961435; 1:100), and H-2Kb/H-2Db (BioLegend, catalog no. 114608, RRID:AB_313599).

Generation of* Tet2- *or* Ifngr1-*KO Cell Lines Using SCAR Technology. *Tet2*- or *Ifngr1*-KO tumor cells were generated using SCAR, a novel lentiviral system that eliminates immunogenic CRISPR-associated neoantigens from virally transduced cell lines. sgRNAs targeting *Tet2* or *Ifngr1* were designed using an online tool (www.benchling.com/crispr). sgRNA sequences are listed in Supplementary Table S3. To package the SCAR-Cas9 lentivirus, HEK293T cells were cotransfected with pSCAR-Cas9-hygro_GFP (ref. 61; Addgene, catalog no. 162075, RRID:Addgene_162075), psPAX2 (Addgene, catalog no. 12260, RRID:Addgene_12260), and pMD2.G (Addgene, catalog no. 12259, RRID:Addgene_12259), introduced via X-tremeGene 9 DNA Transfection Reagent (Roche, catalog no. XTG9-RO). Viral medium was collected for three days, filtered, and stored at 4°C. On the third day, 2,205 cells were incubated with filtered viral medium and 4 μg/mL polybrene (MilliporeSigma, catalog no. TR-1003). At 24 and 48 hours after infection, the medium was replaced with fresh viral medium. Cells were negatively selected with hygromycin (200 μg/mL) over the course of one week, after which GFP-positive cells were isolated by flow cytometry. SCAR–Cas9-expressing cells were transduced with lentivirus containing pSCAR_sgRNA_pruo-mkate-lox2272 (Addgene, catalog no. 162076, RRID:Addgene_162076) vectors ligated with either *Tet2*- or *Ifngr1*-specific sgRNA or a control vector (prepared as described above). Successfully transduced cells were selected with puromycin (2 μg/mL) over the course of five days before GFP/mKate2 double-positive cells were isolated by flow cytometry. We then floxed out the CRISPR-associated neoantigens by transfecting HEK293T cells with a modified psPAX2 (psPAX2_D64V, Addgene_63586, RRID:Addgene_63586) to produce a nonintegrative Cre-expressing lentivirus, which was administered to both the sgControl and sg*Tet2*-1, sg*Tet2*-2, and sg*Ifngr1* cells continuously for three days. Ten days following *Cre* transduction, GFP/mKate2 double-negative cells were isolated by flow cytometry. *Tet2*- or *Ifngr1*-KOs were confirmed by Sanger sequencing of genomic DNA, RT-PCR, or immunoblotting. Successful removal of CRISPR-associated neoantigens was confirmed by Western blotting with a Cas9-specific antibody (Cell Signaling Technology, catalog no. 14697, RRID:AB_2750916; 1:1,000).

Syngeneic Tumor Models, Treatment, and Analysis

***In Vivo* Implantation and Growth Monitoring of Tumor Cells.** Cultured tumor cells were dissociated into single-cell suspensions with 0.25% Trypsin (GIBCO) and rinsed twice with D-PBS (GIBCO), counted, and suspended in a 1:1 mixture of D-PBS (GIBCO) and growth factor–reduced matrigel (Corning). Mice for subcutaneous models were briefly anesthetized and injected subcutaneously on the rear flank with 1×10^6 ICC cells. These studies used the following GEMM-derived cell lines: the CKI^{R132C} cell lines, 2205, or any of its genetically engineered derivatives (2275-4 and 4411), or the CKP cell line, 215, or 254. Once tumors were observed to reach 100 mm^3 in volume, animal groups were randomized, and treatment was administered by group. During subcutaenous tumor experiments, tumor growth was monitored twice a week by measuring tumor size with a digital caliper, and tumor volume was calculated with the formula length × $width^2$, where the shorter of the two measurements was used as width. In accordance with institutional guidelines, mice with

masses measuring >20 mm in diameter were euthanized. For orthotopic allograft models, mice were anesthetized under 2.5% isoflurane and injected with 1×10^6 tumor cells directly to the lobe of the liver using the CKI^{R132C} cell lines 2205 and 2275-4. Following injection, the peritoneum and skin were sutured with silk (5-0G, Ethilon). In pilot studies, mice were euthanized at serial time points to define the kinetics of engraftment and growth of the orthotopic tumors and thereby determine the time after injection to begin treatment studies using these models. These studies established that orthotopic tumors of size 150 cm^3 developed by 10 days, which was subsequently selected as the start point for therapeutic studies. Researchers were not blinded throughout conducting the experiments. Tumor growth was not affected by sex of the host mouse.

AG120 Monotherapy. Five days following subcutaneous or orthotopic tumor cell inoculation, groups of wild-type littermates, C57BL/6/129SF1, or NOD-scid ilr2$^{-/-}$ mice were administered either: (i) vehicle preparation of 0.5% Methyl Cellulose (cP 400) + 4.5% HPMC-ACS + 0.2% Tween 80 in water b.i.d. via oral gavage or (ii) AG120 (Agios Pharmaceuticals) administered b.i.d. via oral gavage at a dose of 150 mg/kg. For GEMMs for AG120 treatment, in pilot studies, CKI^{R132C} mice were euthanized at serial time points to define the kinetics of tumor formation. Mice were monitored for palpable tumor at 40 to 45 weeks to determine the time to begin AG120 treatment. The administration of AG120 followed the statement above. Following the completion of the planned treatment regimen, all tumor samples were collected for further analysis within one hour of final dosage.

AG120 Efficacy following CD8 Depletion. Anti-CD8β antibody (Bio X Cell, catalog no. BE0223, RRID:AB_2687706) or IgG1 isotype control (200 μg per mice; Bio X Cell, catalog no. BE0088, RRID: AB_1107775) was administered (200 μg per mouse) by intraperitoneal injection three days prior to inoculation with tumor cells and was continued at the same dose once every four days throughout treatment. Five days following subcutaenous tumor cell inoculation, mice were administered AG120 therapy as described above.

Combination AG120/Anti–PD-1 Immune Checkpoint Blockade Therapy. Seven days after inoculation, mice were randomized to receive one of the following regimens: (i) vehicle (described above) followed by IgG1 isotype control (200 μg per mice, Bio X Cell, catalog no. BE0088, RRID:AB_1107775) injected intraperitoneally starting at day 0 and continuing once every three days; (ii) AG120 administered b.i.d. via oral gavage at 150 mg/kg followed by intraperitoneal injection of IgG1 isotype starting at day 0 and continuing once every three days; (iii) vehicle followed by one 200 mg dose of anti–PD-1 antibody (Bio X Cell, catalog no. BE0146, RRID:AB_10949053) injected intraperitoneally at day 0 and continuing once every three days; or (iv) AG120 administered b.i.d. via oral gavage at 150 mg/kg followed by intraperitoneal injection of 100 μg anti–PD-1 antibody starting at day 0 and continuing once every three days.

Combination AG120/Anti–PD-1 Immune Checkpoint Blockade Therapy. Five days following subcutaneous tumor inoculation, mice were randomized to receive one of the following regimens: (i) vehicle (described above) followed by 200 μg of IgG2b isotype control (Bio X Cell, catalog no. BE0086, RRID:AB_1107791) injected intraperitoneally starting at day 0 and continuing once every three days; (ii) AG120 administered b.i.d. via oral gavage at 150 mg/kg followed by intraperitoneal injection of IgG1 isotype starting at day 0 and continuing once every three days; (iii) vehicle followed by one 200 μg dose of anti-CTLA4 antibody (Bio X Cell, catalog no. BE0164, RRID:AB_10949609) injected intraperitoneally at day 0 and continuing once every three days; and (iv) AG120 administered b.i.d. via oral gavage at 150 mg/kg followed by intraperitoneal injection of 200 mg anti-CTLA4 antibody starting at day 0 and continuing once every three days.

Immune Memory Rechallenges. Tumor-naïve immunocompetent wild-type mice and mice cured by the AG120 + anti-CTLA4 therapy 125 days after primary challenge were injected subcutaneously with 1×10^6 cells, using a CKI^{R132C} primary ICC cells (the 2205 cell line). Mice were monitored for serial changes in tumor volume for 50 days or until tumor burden required euthanasia.

Luminex Cytokine Assay. Media from cultures were collected and stored at –80°C. Before testing, the conditioned media were thawed on ice. The media were tested with MILLIPLEX MAP Mouse Cytokine/Chemokine Magnetic Bead Panel kit (Millipore, catalog no. MCYTMAG-70K-PX32) according to the manufacturer's instructions. The data were analyzed with MILLIPLEX Analyst software. Fold changes relative to the control were calculated and plotted as $\log_2$ fold change. Lower and upper limits of quantitation (LLOQ/ULOQ) were imputed from standard curves for cytokines above or below detection.

LC/MC-MS AG-120 Measurement in Plasma and Tumor. The concentrations of AG120 in plasma and tumor samples were determined using LC/MS-MS methods. Tumor samples were homogenized using a FastPrep homogenizer for 60 seconds, with 10 volumes (v/w) of methanol:water (80:20 v/v) to get a homogenate with a dilution factor of 11. Calibration standards and QC samples were prepared in blank mouse plasma. A 10-μL aliquot of calibration standards, QCs, unknown plasma, and tumor homogenate were mixed with 200 μL of acetonitrile containing the internal standard (IS) AGI-0018070 (25 ng/mL) for protein precipitation. The mixture was vortexed at 800 rpm for 4 minutes and centrifuged at 4,000 rpm for 10 minutes at 4°C. A 100-μL aliquot of supernatant was mixed with 100 μL of water, vortexed, and then analyzed on an SCIEX Triple Quad 6500+ with an Exion LC AD system. A reversed-phase gradient method using a Waters ACQUITY UPLC HSS T3 Column (100Ã, 1.8 μm, 2.1 mm × 50 mm) maintained at 50°C, provided chromatographic separation. Water with 0.1% formic acid and acetonitrile with 0.1% formic acid were used as mobile phases A and B, respectively, at a total flow rate of 600 μL/minute. AG-120 and IS were ionized under a positive ion electrospray mode and detected through the multiple-reaction monitoring transitions of m/z 583.2/214.0 and m/z 587.3/214.0. Data were acquired using Analyst 1.6.3 (AB Sciex). The standard curve had a coefficient of determination (R^2) value >0.98 in a linear regression with $1/\chi^2$ weighting. The QC samples had a precision and accuracy within 20% of theoretical values. The peak area ratios of analyte relative to IS were used for AG-120 quantitation. Linearity was achieved in the AG-120 concentration range from 1 to 30,000 ng/mL.

GC-MS Analysis for Total 2HG. The method was adapted from Elia and colleagues (83). 2HG stock solution (10 mg/mL) was prepared in water. Glutaric acid stock solution (1 mg/mL) was also prepared in water. Glutaric acid stock solution (75 μL) was premixed with 30 mL of milli-Q water and 50 mL of methanol (extraction solvent 1, ES1), and was stored at –20°C until extraction. Chloroform was prechilled at –20°C until extraction (extraction solvent 2, ES2). Calibration standards were prepared by serial dilution of 2HG stock solution by using methanol and dried by using speedvac, and 800 μL of ES1 and 500 μL of ES2 were added to 20 μL of culture media samples or cell pellet samples. Samples were vortexed for 10 minutes and centrifuged for 10 minutes at 21,300 relative centrifugal force (rcf). Upper phase was collected and transferred to new microtubes and dried by using speedvac. Methoxyamine hydrochloride solution (MOX; 20 mg/mL) was freshly prepared in pyridine. MOX (15 μL) was added to each dried sample, and samples were resuspended in MOX, vortexed and spun down, and heated at 37°C for 90 minutes. TBDMS (30 μL) was added to each dried sample. Samples were vortexed, heated at 60°C for 60 minutes, and centrifuged for 5 minutes at 21,300 rcf. Supernatant was transferred to glass inserts and was analyzed by using GC-MS.

An Agilent 7890B GC system was coupled to an Agilent 5977B single quadrupole mass spectrometer equipped with an electron ionization source. Automated injections were performed with an Agilent 7693 autosampler. The injector temperature was held constant at 270°C. Injections of 1 μL were made in splitless mode. Chromatography was performed on an HP-5ms Ultra Inert Column (30 m × 0.25 mm, 0.25 μm film thickness, Agilent). Helium carrier gas was used at a constant flow of 1 mL/minutes. At the beginning of the experiments, the GC oven temperature program was 100°C initial temperature with 3 minutes hold time and ramping at 2.5°C/minute to a final temperature of 300°C with 2 minutes hold time. After that, in order to reduce the run time, the GC oven temperature program was modified to be 100°C initial temperature with 3 minutes hold time and ramping at 10°C/minute to a final temperature of 300°C with 12 minutes hold time. The transfer line temperature was 250°C, and the source temperature was 230°C. After a solvent delay of 5.5 minutes, mass spectra were acquired at 2.9 scans/second with a mass range of 50 to 550 m/z. Data processing was performed with MassHunter Workstation Software Quantitative Analysis (Version B.09.00/Build 9.0.647.0) for GC-MS and LC-MS.

Enzymatic Measurement of (R)-2HG in GEMM Livers. Liver samples (10 mg) were collected from 11-week-old CK, CKI^{R132C}, and CKI^{R132H} mice immediately following euthanasia. Tissue samples were snap-frozen and stored at −80°C. Enzymatic measurement of (R)-2HG was performed using the BioVision Colorimetric D-2-Hydroxyglutarate [D2HG/(R)-2HG] Assay Kit (BioVision, catalog no. K213) according to the manufacturer's protocol with slight modification. In brief, samples were thawed, suspended in 100 mL of ice-cold D2HG Assay Buffer, and mechanically disrupted. After a 10-minute incubation on ice, samples were centrifuged at 10,000 × *g*, 4°C for 5 minutes, and the supernatant was collected for separation of small-molecule fraction by Amicon low-molecular-weight cutoff filter (Millipore Sigma, catalog no. UFC201024). Each sample (30 mL) was added to three wells of a 96-well plate and designated either internal control, sample, or background. (R)-2HG enzyme was administered to the internal control and sample wells, whereas a blank was added to the background well. The internal control was dosed with 5 nmol of (R)-2HG, and the samples were incubated for one hour at 37°C. Samples were measured using a spectrophotometer OD_{450nm}, and (R)-2HG amount was calculated by subtracting the $OD_{background}$ from each sample and using following the equation:

$$(\mathrm{R})\text{-}2\mathrm{HG}\,(\mathrm{nmol/L}) = \left(\frac{\mathrm{OD}_{\,\mathrm{sample}}}{\mathrm{OD450}_{\mathrm{int.ctrl}} - \mathrm{OD450}_{\,\mathrm{sample}}}\right) \times 5.$$

Quantification and Statistical Analysis

Semiautomated IHC Quantification. Scanned IHC slides were analyzed using QuPath, a free, open-source software for bioimaging analysis (https://qupath.github.io). Depending on the size of tissue, 5 to 10 different 1,600-μm² areas (40× magnification field) of each tumor that exhibited clear ICC phenotypes and were free of necrosis were selected. Signal-positive cells were quantitated by automated positive cell selection analysis at a fixed threshold and maximum background intensity across all samples. HPF was calculated by averaging these values for each sample.

Quantification and Statistical Analysis. Statistical tests were performed with GraphPad Prism software. An unpaired two-tailed Student *t* test was used to determine significant difference between two variables (Figs. 1C, 2D–2G, 2I–2L, 3D, 3F, 4A–4G, 5B–5G, 5K, 6A–6E, and 6G; Supplementary Figs. S1B, S3C, S3D, S3I–S3L, S3N–S3R, S4G–S4H, S5A–S5G, S5J–S5L, S6A, S6D–S6E, S7A, S7D–S7L, S7O–S7R, S8A–S6B, S8D, and S8G). Log-rank test was used to determine statistically significant differences between two or more Kaplan–Meier survival curves (Figs. 1D and 6J; Supplementary Figs. S1D, S1E, and S8I). *, $P < 0.05$; **, $P < 0.01$; ***, $P < 0.001$; ****, $P < 0.0001$; ns, $P > 0.05$. Statistics were performed, and graphs were generated in Prism v9.10 (GraphPad).

GSEA. To test whether gene sets were enriched in response to different conditions, we utilized GSEA MsigDB for Hallmark gene signatures (81, 82) and the liver-specific gene set "HSIAO_LIVER_SPECIFIC_GENES" (ref. 84; http://software.broadinstitute.org/gsea/msigdb) as well as a gene list of HNF4α target genes from TRANSFAC Predicted Transcription Factor Targets (http://gene-regulation.com/; Supplementary Table S5; ref. 85). Hallmarks with enrichment scores greater than 1.7 and possessing an FDR $q < 0.2$ were considered significantly enriched.

Authors' Disclosures

L. Shi reports grants from the NCI and the Cholangiocarcinoma Foundation during the conduct of the study. R.W. Jenkins reports other support from Xsphera Biosciences and Monopteros Therapeutics outside the submitted work. L. Goyal serves as a consultant or advisory board member for Alentis Therapeutics AG, Black Diamond, Basilea, Exelixis, H3Biomedicine, Incyte Corporation, QED Therapeutics, Servier, Sirtex Medical Ltd., Taiho Oncology Inc., and as a consultant or advisory board member for Data Safety Monitoring Committees for AstraZeneca, and reports receiving grant/research support (to institution) from Adaptimmune, Bayer, Eisai, Merck, Macrogenics, Genentech, Novartis, Incyte, Eli Lilly, Loxo Oncology, Relay Therapeutics, QED Therapeutics, Taiho Oncology, Leap Therapeutics, Bristol Meyers Squibb, Nucana, and Servier. B. Nicolay was an employee of and stock holder in Agios Pharmaceuticals during the time this work was carried out. R.T. Manguso reports grants from Calico Life Sciences LLC and personal fees from Bristol Myers Squibb outside the submitted work. N. Bardeesy reports grants and personal fees from Agios Pharmaceuticals, and grants from the NIH/NCI, TargetCancer, ProjectLiv, and the Cholangiocarcinoma Foundation during the conduct of the study. No disclosures were reported by the other authors.

Authors' Contributions

M.-J. Wu: Conceptualization, data curation, formal analysis, validation, investigation, visualization, methodology, writing–original draft, project administration, writing–review and editing. **L. Shi:** Conceptualization, data curation, formal analysis, validation, investigation, visualization, methodology, writing–original draft, writing–review and editing. **J. Dubrot:** Conceptualization, resources, formal analysis, investigation, visualization, methodology, writing–original draft, writing–review and editing. **J. Merritt:** Formal analysis and validation. **V. Vijay:** Validation. **T.-Y. Wei:** Validation and methodology. **E. Kessler:** Data curation, software, formal analysis, validation, investigation, visualization, and methodology. **K.E. Olander:** Data curation, software, formal analysis, validation, investigation, visualization, and methodology. **R. Adil:** Validation. **A. Pankaj:** Formal analysis, validation, investigation, and methodology. **K.S. Tummala:** Writing–review and editing. **V. Weeresekara:** Writing–review and editing. **Y. Zhen:** Writing–review and editing. **Q. Wu:** Writing–review and editing. **M. Luo:** Investigation and methodology. **W. Shen:** Visualization. **M. Garcia-Beccaria:** Validation and investigation. **M. Fernandez-Vaquero:** Validation and investigation. **C. Hudson:** Formal analysis, validation, investigation, and methodology. **S. Ronseaux:** Formal analysis, validation, investigation, visualization, and methodology. **Y. Sun:** Investigation and methodology. **R. Saad-Berreta:** Validation and investigation. **R.W. Jenkins:** Methodology, writing–review and editing. **T. Wang:** Formal analysis, investigation, and methodology. **M. Heikenwalder:** Writing–review and editing. **C.R. Ferrone:** Resources, writing–review and editing. **L. Goyal:** Resources, writing–review and editing. **B. Nicolay:** Resources.

V. Deshpande: Resources, formal analysis, and validation. **R.M. Kohli:** Methodology, writing–review and editing. **H. Zheng:** Resources. **R.T. Manguso:** Conceptualization, resources, supervision, visualization, methodology, writing–original draft, writing–review and editing. **N. Bardeesy:** Conceptualization, resources, supervision, funding acquisition, methodology, writing–original draft, project administration, writing–review and editing.

Acknowledgments

This work was supported by the following sources: NCI SPORE P50 CA127003, the Gallagher Chair in Gastrointestinal Cancer Research, ProjectLiv, the TargetCancer Foundation, the Massachusetts Life Sciences Center, the Samuel Waxman Cancer Research Foundation (to N. Bardeesy), and NIH R01-HG010646 (to R.M. Kohli). M.-J. Wu is supported by a Cholangiocarcinoma Foundation Postdoctoral Fellowship and an American Cancer Society Postdoctoral Fellowship PF-20-136-01-TBG. L. Shi is supported by a Cholangiocarcinoma Foundation Christopher J. Wilke Memorial Research Fellowship, the MGH Fund for Discovery, an MGH Excellence Award, NCI K99CA245194, and NCI SPORE P50CA127003. The authors thank C.-J. Lio, W.-L. Wang, R. Mostoslavsky, W.Y. Kim, L. Ellisen, and A.X. Zhu for their critical reading of the manuscript.

The costs of publication of this article were defrayed in part by the payment of page charges. This article must therefore be hereby marked *advertisement* in accordance with 18 U.S.C. Section 1734 solely to indicate this fact.

Received August 10, 2021; revised October 29, 2021; accepted November 23, 2021; published first November 30, 2021.

REFERENCES

1. Borger DR, Tanabe KK, Fan KC, Lopez HU, Fantin VR, Straley KS, et al. Frequent mutation of isocitrate dehydrogenase (IDH)1 and IDH2 in cholangiocarcinoma identified through broad-based tumor genotyping. Oncol 2012;17:72–9.
2. Waitkus MS, Diplas BH, Yan H. Biological role and therapeutic potential of IDH mutations in cancer. Cancer Cell 2018;34:186–95.
3. Ye D, Guan K-L, Xiong Y. Metabolism, activity, and targeting of D- and L-2-hydroxyglutarates. Trends Cancer 2018;4:151–65.
4. Lowery MA, Ptashkin RN, Jordan EJ, Berger MF, Zehir A, Capanu M, et al. Comprehensive molecular profiling of intra- and extrahepatic cholangiocarcinomas: potential targets for intervention. Clin Cancer Res 2018;24:4154–61.
5. Ward PS, Patel J, Wise DR, Abdel-Wahab O, Bennett BD, Coller HA, et al. The common feature of leukemia-associated IDH1 and IDH2 mutations is a neomorphic enzyme activity converting α-ketoglutarate to 2-hydroxyglutarate. Cancer Cell 2010;17:225–34.
6. Dang L, White DW, Gross S, Bennett BD, Bittinger MA, Driggers EM, et al. Cancer-associated IDH1 mutations produce 2-hydroxyglutarate. Nature 2009;462:739–44.
7. Xu W, Yang H, Liu Y, Yang Y, Wang P, Kim S-H, et al. Oncometabolite 2-hydroxyglutarate is a competitive inhibitor of α-ketoglutarate-dependent dioxygenases. Cancer Cell 2011;19:17–30.
8. Losman JA, Koivunen P, Kaelin WG. 2-Oxoglutarate-dependent dioxygenases in cancer. Nat Rev Cancer 2020;20:710–26.
9. Chowdhury R, Yeoh KK, Tian Y, Hillringhaus L, Bagg EA, Rose NR, et al. The oncometabolite 2-hydroxyglutarate inhibits histone lysine demethylases. Embo Rep 2011;12:463–9.
10. Figueroa ME, Abdel-Wahab O, Lu C, Ward PS, Patel J, Shih A, et al. Leukemic IDH1 and IDH2 mutations result in a hypermethylation phenotype, disrupt TET2 function, and impair hematopoietic differentiation. Cancer Cell 2010;18:553–67.
11. McBrayer SK, Mayers JR, DiNatale GJ, Shi DD, Khanal J, Chakraborty AA, et al. Transaminase inhibition by 2-hydroxyglutarate impairs glutamate biosynthesis and redox homeostasis in glioma. Cell 2018;175:101–16.
12. Sasaki M, Knobbe CB, Itsumi M, Elia AJ, Harris IS, Chio IIC, et al. D-2-hydroxyglutarate produced by mutant IDH1 perturbs collagen maturation and basement membrane function. Gene Dev 2012; 26:2038–49.
13. Wang P, Wu J, Ma S, Zhang L, Yao J, Hoadley KA, et al. Oncometabolite D-2-hydroxyglutarate inhibits ALKBH DNA repair enzymes and sensitizes IDH mutant cells to alkylating agents. Cell Rep 2015;13:2353–61.
14. Sulkowski PL, Oeck S, Dow J, Economos NG, Mirfakhraie L, Liu Y, et al. Oncometabolites suppress DNA repair by disrupting local chromatin signalling. Nature 2020;582:586–91.
15. Carbonneau M, Gagné LM, Lalonde ME, Germain MA, Motorina A, Guiot MC, et al. The oncometabolite 2-hydroxyglutarate activates the mTOR signalling pathway. Nat Commun 2016;7:12700.
16. Koivunen P, Lee S, Duncan CG, Lopez G, Lu G, Ramkissoon S, et al. Transformation by the (R)-enantiomer of 2-hydroxyglutarate linked to EGLN activation. Nature 2012;483:484–8.
17. Kohanbash G, Carrera DA, Shrivastav S, Ahn BJ, Jahan N, Mazor T, et al. Isocitrate dehydrogenase mutations suppress STAT1 and CD8+ T cell accumulation in gliomas. J Clin Invest 2017;127:1425–37.
18. Bunse L, Pusch S, Bunse T, Sahm F, Sanghvi K, Friedrich M, et al. Suppression of antitumor T cell immunity by the oncometabolite (R)-2-hydroxyglutarate. Nat Med 2018;24:1192–203.
19. Amankulor NM, Kim Y, Arora S, Kargl J, Szulzewsky F, Hanke M, et al. Mutant IDH1 regulates the tumor-associated immune system in gliomas. Gene Dev 2017;31:774–86.
20. Leca J, Fortin J, Mak TW. Illuminating the cross-talk between tumor metabolism and immunity in IDH-mutated cancers. Curr Opin Biotech 2021;68:181–5.
21. Ward PS, Lu C, Cross JR, Abdel-Wahab O, Levine RL, Schwartz GK, et al. The potential for isocitrate dehydrogenase mutations to produce 2-hydroxyglutarate depends on allele specificity and subcellular compartmentalization. J Biol Chem 2013;288:3804–15.
22. Lemonnier F, Cairns RA, Inoue S, Li WY, Dupuy A, Broutin S, et al. The IDH2 R172K mutation associated with angioimmunoblastic T-cell lymphoma produces 2HG in T cells and impacts lymphoid development. Proc Natl Acad Sci U S A 2016;113:15084–9.
23. Saha SK, Parachoniak CA, Ghanta KS, Fitamant J, Ross KN, Najem MS, et al. Mutant IDH inhibits HNF-4α to block hepatocyte differentiation and promote biliary cancer. Nature 2014;513:110–4.
24. DiNardo CD, Stein EM, de Botton S, Roboz GJ, Altman JK, Mims AS, et al. Durable remissions with ivosidenib in IDH1-mutated relapsed or refractory AML. New Engl J Med 2018;378:2386–98.
25. Intlekofer AM, Shih AH, Wang B, Nazir A, Rustenburg AS, Albanese SK, et al. Acquired resistance to IDH inhibition through trans or cis dimer-interface mutations. Nature 2018;559:125–9.
26. Stein E, Yen K. Targeted differentiation therapy with mutant IDH inhibitors: early experiences and parallels with other differentiation agents. Annu Rev Cancer Biol 2017;1:379–401.
27. Wang F, Travins J, DeLaBarre B, Penard-Lacronique V, Schalm S, Hansen E, et al. Targeted inhibition of mutant IDH2 in leukemia cells induces cellular differentiation. Science 2013;340:622–6.
28. Yen K, Travins J, Wang F, David MD, Artin E, Straley K, et al. AG-221, a first-in-class therapy targeting acute myeloid leukemia harboring oncogenic IDH2 mutations. Cancer Discov 2017;7:478–93.
29. Amary MF, Bacsi K, Maggiani F, Damato S, Halai D, Berisha F, et al. IDH1 and IDH2 mutations are frequent events in central chondrosarcoma and central and periosteal chondromas but not in other mesenchymal tumours. J Pathol 2011;224:334–43.
30. Yan H, Parsons DW, Jin G, McLendon R, Rasheed BA, Yuan W, et al. IDH1 and IDH2 mutations in gliomas. N Engl J Med 2009;360: 765–73.
31. Lu C, Ward PS, Kapoor GS, Rohle D, Turcan S, Abdel-Wahab O, et al. IDH mutation impairs histone demethylation and results in a block to cell differentiation. Nature 2012;483:474–8.
32. Abou-Alfa GK, Macarulla T, Javle MM, Kelley RK, Lubner SJ, Adeva J, et al. Ivosidenib in IDH1-mutant, chemotherapy-refractory cholangiocarcinoma (ClarIDHy): a multicentre, randomised, double-blind, placebo-controlled, phase 3 study. Lancet Oncol 2020;21:796–807.

33. Mellinghoff IK, Ellingson BM, Touat M, Maher E, Fuente MIDL, Holdhoff M, et al. Ivosidenib in isocitrate dehydrogenase 1–mutated advanced glioma. J Clin Oncol 2020;38:3398–406.
34. Zhu AX, Macarulla T, Javle MM, Kelley RK, Lubner SJ, Adeva J, et al. Final results from ClarIDHy, a global, phase III, randomized, double-blind study of ivosidenib (IVO) versus placebo (PBO) in patients (pts) with previously treated cholangiocarcinoma (CCA) and an isocitrate dehydrogenase 1 (IDH1) mutation. J Clin Oncol 39, 2021 (suppl 3; abstr 266).
35. Johannessen TCA, Mukherjee J, Viswanath P, Ohba S, Ronen SM, Bjerkvig R, et al. Rapid conversion of mutant IDH1 from driver to passenger in a model of human gliomagenesis. Am Assoc Cancer Res 2016;14:976–83.
36. Mazor T, Chesnelong C, Pankov A, Jalbert LE, Hong C, Hayes J, et al. Clonal expansion and epigenetic reprogramming following deletion or amplification of mutant IDH1. Proc Natl Acad Sci U S A 2017;114:10743–8.
37. Moure CJ, Diplas BH, Chen LH, Yang R, Pirozzi CJ, Wang Z, et al. CRISPR editing of mutant IDH1 R132H induces a CpG methylation-low state in patient-derived glioma models of G-CIMP. Mol Cancer Res 2019;17:2042–50.
38. Núñez FJ, Mendez FM, Kadiyala P, Alghamri MS, Savelieff MG, Garcia-Fabiani MB, et al. IDH1-R132H acts as a tumor suppressor in glioma via epigenetic up-regulation of the DNA damage response. Sci Transl Med 2019;11:eaaq1427.
39. Inoue S, Li WY, Tseng A, Beerman I, Elia AJ, Bendall SC, et al. Mutant IDH1 downregulates ATM and alters DNA repair and sensitivity to DNA damage independent of TET2. Cancer Cell 2016;30:337–48.
40. Sulkowski PL, Corso CD, Robinson ND, Scanlon SE, Purshouse KR, Bai H, et al. 2-Hydroxyglutarate produced by neomorphic IDH mutations suppresses homologous recombination and induces PARP inhibitor sensitivity. Sci Transl Med 2017;9:eaal2463.
41. Tateishi K, Wakimoto H, Iafrate AJ, Tanaka S, Loebel F, Lelic N, et al. Extreme vulnerability of IDH1 mutant cancers to NAD+ depletion. Cancer Cell 2015;28:773–84.
42. Wang Y, Wild AT, Turcan S, Wu WH, Sigel C, Klimstra DS, et al. Targeting therapeutic vulnerabilities with PARP inhibition and radiation in IDH-mutant gliomas and cholangiocarcinomas. Sci Adv 2020;6:eaaz3221.
43. Chan SM, Thomas D, Corces-Zimmerman MR, Xavy S, Rastogi S, Hong WJ, et al. Isocitrate dehydrogenase 1 and 2 mutations induce BCL-2 dependence in acute myeloid leukemia. Nat Med 2015;21:178–84.
44. Gao J, Aksoy BA, Dogrusoz U, Dresdner G, Gross B, Sumer SO, et al. Integrative analysis of complex cancer genomics and clinical profiles using the cBioPortal. Sci Signal 2013;6:pl1.
45. Cerami E, Gao J, Dogrusoz U, Gross BE, Sumer SO, Aksoy BA, et al. The cBio cancer genomics portal: an open platform for exploring multidimensional cancer genomics data. Cancer Discov 2012;2:401–4.
46. The AACR Project GENIE Consortium. AACR Project GENIE: powering precision medicine through an international consortium. Cancer Discov 2017;7:818–31.
47. O'Dell MR, Huang JL, Whitney-Miller CL, Deshpande V, Rothberg P, Grose V, et al. KrasG12D and p53 mutation cause primary intrahepatic cholangiocarcinoma. Cancer Res 2012;72:1557–67.
48. Fan B, Abou-Alfa GK, Zhu AX, Pandya SS, Jia H, Yin F, et al. Pharmacokinetics/pharmacodynamics (PK/PD) of ivosidenib in patients with mutant IDH1 advanced cholangiocarcinoma from the phase III ClarIDHy study. J Clin Oncol 38, 2020 (suppl 4; abstr 539).
49. Anderson KG, Stromnes IM, Greenberg PD. Obstacles posed by the tumor microenvironment to T cell activity: a case for synergistic therapies. Cancer Cell 2017;31:311–25.
50. Hu J, Zhao Q, Kong LY, Wang J, Yan J, Xia X, et al. Regulation of tumor immune suppression and cancer cell survival by CXCL1/2 elevation in glioblastoma multiforme. Sci Adv 2021;7:eabc2511.
51. Li J, Byrne KT, Yan F, Yamazoe T, Chen Z, Baslan T, et al. Tumor cell-intrinsic factors underlie heterogeneity of immune cell infiltration and response to immunotherapy. Immunity 2018;49:178–93.
52. Parker BS, Rautela J, Hertzog PJ. Antitumour actions of interferons: implications for cancer therapy. Nat Rev Cancer 2016;16:131–44.
53. Dutta R, Zhang TY, Köhnke T, Thomas D, Linde M, Gars E, et al. Enasidenib drives human erythroid differentiation independently of isocitrate dehydrogenase 2. J Clin Invest 2020;130:1843–9.
54. Richardson LG, Choi BD, Curry WT. (R)-2-hydroxyglutarate drives immune quiescence in the tumor microenvironment of IDH-mutant gliomas. Transl Cancer Res 2019;8:S167–70.
55. Zhang L, Romero P. Metabolic control of CD8+ T cell fate decisions and antitumor immunity. Trends Mol Med 2018;24:30–48.
56. Miller BC, Sen DR, Abosy RA, Bi K, Virkud YV, LaFleur MW, et al. Subsets of exhausted CD8+ T cells differentially mediate tumor control and respond to checkpoint blockade. Nat Immunol 2019;20:326–36.
57. Sade-Feldman M, Yizhak K, Bjorgaard SL, Ray JP, de Boer CG, Jenkins RW, et al. Defining T cell states associated with response to checkpoint immunotherapy in melanoma. Cell 2018;175:998–1013.
58. Siddiqui I, Schaeuble K, Chennupati V, Marraco SAF, Calderon-Copete S, Ferreira DP, et al. Intratumoral Tcf1+PD-1+CD8+ T cells with stem-like properties promote tumor control in response to vaccination and checkpoint blockade immunotherapy. Immunity 2019;50:195–211.
59. Fujimoto A, Furuta M, Totoki Y, Tsunoda T, Kato M, Shiraishi Y, et al. Whole-genome mutational landscape and characterization of noncoding and structural mutations in liver cancer. Nat Genet 2016;48:500–9.
60. Xu Y, Lv L, Liu Y, Smith MD, Li WC, Tan X, et al. Tumor suppressor TET2 promotes cancer immunity and immunotherapy efficacy. J Clin Invest 2019;129:4316–31.
61. Dubrot J, Lane-Reticker SK, Kessler EA, Ayer A, Mishra G, Wolfe CH, et al. In vivo screens using a selective CRISPR antigen removal lentiviral vector system reveal immune dependencies in renal cell carcinoma. Immunity 2021;54:571–85.
62. Garcia-Diaz A, Shin DS, Moreno BH, Saco J, Escuin-Ordinas H, Rodriguez GA, et al. Interferon receptor signaling pathways regulating PD-L1 and PD-L2 expression. Cell Rep 2017;19:1189–201.
63. Togashi Y, Shitara K, Nishikawa H. Regulatory T cells in cancer immunosuppression—implications for anticancer therapy. Nat Rev Clin Oncol 2019;16:356–71.
64. Weinberg SE, Singer BD, Steinert EM, Martinez CA, Mehta MM, Martínez-Reyes I, et al. Mitochondrial complex III is essential for suppressive function of regulatory T cells. Nature 2019;565:495–9.
65. Simpson TR, Li F, Montalvo-Ortiz W, Sepulveda MA, Bergerhoff K, Arce F, et al. Fc-dependent depletion of tumor-infiltrating regulatory T cells co-defines the efficacy of anti–CTLA-4 therapy against melanoma. J Exp Med 2013;210:1695–710.
66. Foskolou IP, Barbieri L, Vernet A, Bargiela D, Cunha PP, Velica P, et al. The S enantiomer of 2-hydroxyglutarate increases central memory CD8 populations and improves CAR-T therapy outcome. Blood Adv 2020;4:4483–93.
67. Tyrakis PA, Palazon A, Macias D, KianL LP, Anthony T, Veliça P, et al. S-2-hydroxyglutarate regulates CD8+ T-lymphocyte fate. Nature 2016;540:236–41.
68. Kamada T, Togashi Y, Tay C, Ha D, Sasaki A, Nakamura Y, et al. PD-1+ regulatory T cells amplified by PD-1 blockade promote hyperprogression of cancer. Proc Natl Acad Sci U S A 2019;116:201822001.
69. Rowshanravan B, Halliday N, Sansom DM. CTLA-4: a moving target in immunotherapy. Blood 2018;131:58–67.
70. Aguado-Fraile E, Tassinari A, Ishii Y, Sigel C, Lowery MA, Goyal L, et al. Molecular and morphological changes induced by ivosidenib correlate with efficacy in mutant-IDH1 cholangiocarcinoma. Future Oncol 2021;17:2057–74.
71. Lampl S, Janas MK, Donakonda S, Brugger M, Lohr K, Schneider A, et al. Reduced mitochondrial resilience enables non-canonical induction of apoptosis after TNF receptor signaling in virus-infected hepatocytes. J Hepatol 2020;73:1347–59.
72. Namineni S, O'Connor T, Faure-Dupuy S, Johansen P, Riedl T, Liu K, et al. A dual role for hepatocyte-intrinsic canonical NF-κB signaling in virus control. J Hepatol 2020;72:960–75.
73. Mahadevan NR, Knelson EH, Wolff JO, Vajdi A, Saigi M, Campisi M, et al. Intrinsic immunogenicity of small cell lung carcinoma revealed by its cellular plasticity. Cancer Discov 2021;11:1952–69.
74. Fitamant J, Kottakis F, Benhamouche S, Tian HS, Chuvin N, Parachoniak CA, et al. YAP inhibition restores hepatocyte

differentiation in advanced HCC, leading to tumor regression. Cell Rep 2015;10:1692–707.
75. Yang H, Wang H, Jaenisch R. Generating genetically modified mice using CRISPR/Cas-mediated genome engineering. Nat Protoc 2014;9:1956–68.
76. Aizarani N, Saviano A, Sagar , Mailly L, Durand S, Herman JS, et al. A human liver cell atlas reveals heterogeneity and epithelial progenitors. Nature 2019;572:199–204.
77. MacParland SA, Liu JC, Ma X-Z, Innes BT, Bartczak AM, Gage BK, et al. Single cell RNA sequencing of human liver reveals distinct intrahepatic macrophage populations. Nat Commun 2018;9:4383.
78. Wolf FA, Angerer P, Theis FJ. SCANPY: large-scale single-cell gene expression data analysis. Genome Biol 2018;19:15.
79. Korsunsky I, Millard N, Fan J, Slowikowski K, Zhang F, Wei K, et al. Fast, sensitive and accurate integration of single-cell data with Harmony. Nat Methods 2019;16:1289–96.
80. Ntranos V, Yi L, Melsted P, Pachter L. A discriminative learning approach to differential expression analysis for single-cell RNA-seq. Nat Methods 2019;16:163–6.
81. Subramanian A, Tamayo P, Mootha VK, Mukherjee S, Ebert BL, Gillette MA, et al. Gene set enrichment analysis: a knowledge-based approach for interpreting genome-wide expression profiles. Proc Natl Acad Sci U S A 2005;102:15545–50.
82. Mootha VK, Lindgren CM, Eriksson K-F, Subramanian A, Sihag S, Lehar J, et al. PGC-1α-responsive genes involved in oxidative phosphorylation are coordinately downregulated in human diabetes. Nat Genet 2003;34:267–73.
83. Elia I, Broekaert D, Christen S, Boon R, Radaelli E, Orth MF, et al. Proline metabolism supports metastasis formation and could be inhibited to selectively target metastasizing cancer cells. Nat Commun 2017;8:15267.
84. Hsiao LL, Dangond F, Yoshida T, Hong R, Jensen RV, Misra J, et al. A compendium of gene expression in normal human tissues. Physiol Genomics 2001;7:97–104.
85. Matys V, Kel-Margoulis OV, Fricke E, Liebich I, Land S, Barre-Dirrie A, et al. TRANSFAC® and its module TRANSCompel®: transcriptional gene regulation in eukaryotes. Nucleic Acids Res 2006;34:D108–10.